Simulations of dilute sedimenting suspensions at finite-particle Reynolds numbers

R. Sungkorn and J. J. Derksen

Citation: Phys. Fluids **24**, 123303 (2012); doi: 10.1063/1.4770310
View online: http://dx.doi.org/10.1063/1.4770310
View Table of Contents: http://pof.aip.org/resource/1/PHFLE6/v24/i12
Published by the American Institute of Physics.

PHYSICS OF FLUIDS **24**, 123303 (2012)

Simulations of dilute sedimenting suspensions at finite-particle Reynolds numbers

R. Sungkorn and J. J. Derksen
Department of Chemical and Materials Engineering, University of Alberta, Edmonton, Alberta T6G 2G6, Canada

(Received 1 May 2012; accepted 6 November 2012; published online 13 December 2012)

An alternative numerical method for suspension flows with application to sedimenting suspensions at finite-particle Reynolds numbers Re_p is presented. The method consists of an extended lattice-Boltzmann scheme for discretizing the locally averaged conservation equations and a Lagrangian particle tracking model for tracking the trajectories of individual particles. The method is able to capture the main features of the sedimenting suspensions with reasonable computational expenses. Experimental observations from the literature have been correctly reproduced. It is numerically demonstrated that, at finite Re_p, there exists a range of domain sizes in which particle velocity fluctuation amplitudes $\langle \Delta V_{\parallel,\perp} \rangle$ have a strong domain size dependence, and above which the fluctuation amplitudes become weakly dependent. The size range strongly relates with Re_p and the particle volume fraction ϕ_p. Furthermore, a transition in the fluctuation amplitudes is found at Re_p around 0.08. The magnitude and length scale dependence of the fluctuation amplitudes at finite Re_p are well represented by introducing new fluctuation amplitude scaling functions $C_{1,(\parallel,\perp)}(Re_p, \phi_p)$ and characteristic length scaling function $C_2(Re_p, \phi_p)$ in the correlation derived by Segre *et al.* from their experiments at low Re_p ["Long-range correlations in sedimentation," Phys. Rev. Lett. **79**, 2574–2577 (1997)] in the form $\langle \Delta V_{\parallel,\perp} \rangle = \langle V_\parallel \rangle C_{1,(\parallel,\perp)}(Re_p, \phi_p)\phi_p^{1/3}\{1 - \exp[-L/(C_2(Re_p, \phi_p)r_p\phi_p^{-1/3})]\}$. © *2012 American Institute of Physics*. [http://dx.doi.org/10.1063/1.4770310]

I. INTRODUCTION

Sedimenting suspensions exist in various forms of natural phenomena and man-made processes. Examples include the sedimentation of dust in the atmosphere, the centrifugation of proteins, and the deposit of contaminants in waste water. Despite a century of research, a complete understanding of such phenomena is only partially achieved.[1–5]

When a solid spherical particle is placed in a quiescent viscous fluid within an unbounded domain, the particle velocity magnitude increases from zero to a steady value V_t under the influence of gravity. Note that, this paper focuses only on systems with spherical particles. The particle maintains its terminal velocity V_t, since the net force (e.g., the sum of the drag force, buoyancy, and gravity) on the particle is zero. While sedimenting, the particle drags the fluid with it generating a velocity disturbance in the fluid which decays as $O(1/r)$ with r the distance around the particle.[1] By randomly adding identical particles in the domain, a sedimenting suspension of monodisperse particles is formed. The dynamics of the suspension are more complex since they are not characterized solely by the interactions between particle and fluid but also by the direct and indirect interactions between particles. The direct interactions take place in the form of collisions between particles. The indirect interactions are induced by the velocity disturbance in the fluid generated by other particles. The indirect interactions are also known as the long-range multibody hydrodynamic interactions.[1,6] The average particle settling velocity in the direction parallel to gravity $\langle V_\parallel \rangle$ will be smaller than the terminal velocity due to the hydrodynamic interaction, the effect of particles displacing significant amount of fluid, and the buoyancy which now relates to the mixture density. Hereafter $\langle - \rangle$ represents the average value over all particles in the domain. The subscripts $\parallel$ and $\perp$

represent the directions parallel and perpendicular to gravity, respectively. The hindrance in $\langle V_\parallel \rangle$ is well understood by the rigorous theoretical derivation of Batchelor[7] at low particle Reynolds number $Re_p = 2V_t r_p/\nu_l$ (based on the particle radius r_p and the fluid kinematic viscosity ν_l) and low particle volume fraction ϕ_p, and by numerical simulations at higher ϕ_p.[4] The average settling velocity in the direction parallel to gravity $\langle V_\parallel \rangle$ is found to be a function of ϕ_p and well represented by the correlation

$$\langle V_\parallel \rangle = V_t k \left(1 - \phi_p\right)^n , \tag{1}$$

where the values of k and n depend on the Re_p regime[8,9] However, sedimenting suspensions are not characterized completely by the average settling velocity, the amplitude of the particle velocity fluctuations about the average $\langle \Delta V_{\parallel,\perp} \rangle = \langle [V_{\parallel,\perp} - \langle V_{\parallel,\perp} \rangle]^2 \rangle^{1/2}$ is also important, especially in describing the mixing within the suspensions. Despite the universal behavior of the average settling velocities (i.e., $\langle V_{\parallel,\perp} \rangle$ being independent from the size and shape of the container[7,10]), Caflisch and Luke[11] pointed out based on Batchelor's assumptions that the particle velocity fluctuations scale linearly with the size of the container. Similar scaling behavior was found in numerical simulations.[12,13] In contrast, no such dependency was found experimentally.[3,4,6,10] This contradiction, known as Caflisch-Luke paradox, generated controversy among researchers. However, some observations from the experiments at Re_p up to $O(10^{-3})$ play a key role in increasing our understanding of sedimenting suspensions. First, the fluctuation amplitudes $\langle \Delta V_{\parallel,\perp} \rangle$ were found to increase with the particle volume fraction as $\phi_p^{1/3}$ up to $\phi_p = 0.3$, and exhibited strong anisotropy with the greater magnitude in the direction parallel to gravity.[2,6] Second, there exists a range of domain sizes in which $\langle \Delta V_{\parallel,\perp} \rangle$ have a strong domain size dependence, and above which $\langle \Delta V_{\parallel,\perp} \rangle$ become weakly dependent.[2] Remarkably, previous studies focus extensively on the influence of the particle volume fraction ϕ_p and L on the sedimenting suspensions. The influence of finite Re_p has sparked somewhat less interest, first by Hinch[14] and Koch,[15] and recently by Yin and Koch.[5,16]

The objectives of this paper are twofold. First, to propose an alternative numerical simulation method which can be used to gain insight into sedimenting suspensions. A variation of the lattice-Boltzmann (LB) scheme due to Somers,[17] and Eggels and Somers[18] is extended to include the presence of the discrete particle phase in the locally averaged conservation equations.[19] In order to simulate large numbers of particles in large domains for a sufficiently long simulation period, a distributed-particle concept is employed. With the expense of flow details, this approach provides new perspective to the study of sedimenting suspensions which is prohibitively expensive for direct numerical approaches with fully resolved particles. In this concept, the trajectories of individual particles are tracked in a Lagrangian manner by solving Newton's equations of motion. The influences of the particles on the fluid are mimicked through momentum coupling between solid and fluid, and the incorporation of the fluid volume fraction $\phi_l = 1 - \phi_p$ in the conservation equations. Flow features at scales smaller than the particles are lumped in correlations for drag and lift, and in a hindrance function. It is postulated that the distributed-particle concept contains the minimum physics required for realistic numerical simulations of dilute sedimenting suspensions at low and finite Re_p (i.e., $Re_p \leq 2$). This will be assessed by comparing the simulation results with experimental data from the literature.

Second, to numerically investigate the behavior of sedimenting suspensions with particle Reynolds numbers Re_p in the finite range, i.e., $Re_p \sim O(10^{-2})$ to $O(10^0)$. This paper is limited to sedimenting suspensions of non-Brownian monodisperse spherical particles at dilute particle volume fraction, i.e., ϕ_p up to 0.01. Complexities, which may arise from the presence of walls and stratification in the particle concentration, are avoided by considering only cubic periodic domains with statistically uniformly distributed particles.

The paper is organized as follows. In Sec. II, a derivation of the extended lattice-Boltzmann scheme is presented. The distributed-point particle concept is briefly introduced. The proposed numerical method is used to simulate sedimenting suspensions at various particle volume fractions ϕ_p, particle Reynolds numbers Re_p, and domain sizes. In Sec. III, the simulation results are presented and discussed. Comparisons with experimental data from the literature and the validity of the

proposed method are demonstrated. The understandings obtained from the simulations are concluded in Sec. IV.

II. NUMERICAL METHOD

A. Liquid hydrodynamics

Consider a two-phase flow system consisting of dispersed particles in a continuous fluid phase without mass transfer. If the scale of interest is larger than the scale of the dispersed particles, the continuous phase hydrodynamics can be described by averaging properties at an instant in time over a volume. The averaging volume must be chosen such that it is large enough to obtain a near stationary average and small enough to correctly provide the local-averaged values.[19,21] In this paper, the following form of the locally averaged mass conservation equation is used:[20]

$$\partial_t (\phi_l \rho_l) + \nabla \cdot (\phi_l \rho_l \mathbf{u}) = 0, \tag{2}$$

with ϕ_l the continuous fluid phase volume fraction, ρ_l the fluid density, and $\mathbf{u}$ the average velocity of the continuous fluid phase. The locally averaged momentum conservation equation takes the following form:

$$\partial_t (\phi_l \rho_l \mathbf{u}) + \nabla \cdot (\phi_l \rho_l \mathbf{u}\mathbf{u}) = \phi_l \nabla \cdot \sigma - \frac{1}{V_l}\mathbf{F_p}, \tag{3}$$

with $\mathbf{F_p}$ the sum of forces exerted by particles on the fluid and V_l the averaging volume. The stress tensor σ is expressed as

$$\sigma = -P\mathbf{I} + \rho_l \nu_l \left[\nabla \mathbf{u} + (\nabla \mathbf{u})^T - \frac{1}{2}(\nabla \cdot \mathbf{u})\mathbf{I}\right], \tag{4}$$

where P denotes the modified pressure.

In order to extend the existing lattice-Boltzmann scheme for the locally averaged conservation equations presented above, we split the governing equations into a contribution to the single phase flow and a part arising from the presence of the dispersed particles. The equations are rearranged using some standard algebra to

$$\partial_t \rho_l + \nabla \cdot (\rho_l \mathbf{u}) = f^{\phi}, \tag{5}$$

$$\partial_t (\rho_l \mathbf{u}) + \nabla \cdot (\rho_l \mathbf{u}\mathbf{u}) = \nabla \cdot \sigma - \frac{1}{\phi_l V_l}\mathbf{F_p} + f^{\phi}\mathbf{u}. \tag{6}$$

The factor due to the presence of the dispersed phase f^{ϕ} is defined as

$$f^{\phi} = -\frac{\rho_l}{\phi_l}\left[\partial_t \phi_l + \mathbf{u} \cdot \nabla \phi_l\right]. \tag{7}$$

It can be noticed that Eqs. (5) and (6) resemble their single-phase counterparts with an addition of the factor f^{ϕ} and the solid-to-fluid coupling force term.

The lattice-LB scheme mimics the evolution of fluid flow using a many-particle system residing on a uniform, cubic lattice.[22,23] The projection of the four-dimensional (4D) face-centered-hypercubic (FCHC) lattice is commonly used for simulations of the Navier-Stokes equations.[17,24] In this paper, the FCHC lattice is projected with 18 velocity directions $\mathbf{c_i}$ (with i = 1, . . . ,18) for 3D space. The scheme involves two steps: a propagation step in which mass densities N_i at position $\mathbf{x}$ travel to position $\mathbf{x} + \mathbf{c_i}\Delta t$, and a collision step that redistributes the mass densities at each lattice site. These two steps can be described in the form of the lattice-Boltzmann equation (LBE) which is similar to the kinetic equation in lattice-gas automata,[25]

$$N_i (\mathbf{x} + \mathbf{c_i}\Delta t, t + \Delta t) = N_i (\mathbf{x}, t) + \Omega_i (\mathbf{N}), \tag{8}$$

with Δt the time increment in lattice units (usually set to unity), and Ω_i the collision operator which depends nonlinearly on all components of $\mathbf{N}$. The differential form of the LBE can be derived from

a first-order Taylor expansion in time and space,

$$\partial_t N_i + \mathbf{c_i} \cdot \nabla N_i = \Omega_i (\mathbf{N}) . \tag{9}$$

According to the locally averaged conservation equations introduced earlier (Eqs. (5) and (6)), Ω_i is constrained by the following conditions:

$$\sum_i \Omega_i(\mathbf{N}) = f^\phi, \qquad \sum_i \mathbf{c_i}\Omega_i(\mathbf{N}) = \mathbf{f} + \mathbf{u} f^\phi, \tag{10}$$

with $\mathbf{f} = -\mathbf{F_p}/(\phi_l V_l)$. The mass density $\rho_l(\mathbf{x}, t)$ and the momentum concentration $\rho_l(\mathbf{x}, t)\mathbf{u}(\mathbf{x}, t)$ are defined in terms of N_i as

$$\rho_l (\mathbf{x}, t) = \sum_i N_i (\mathbf{x}, t) , \qquad \rho_l (\mathbf{x}, t) \mathbf{u} (\mathbf{x}, t) = \sum_i \mathbf{c_i} N_i (\mathbf{x}, t) . \tag{11}$$

According to statistical mechanics, N_i will evolve toward a local equilibrium at low Mach number. Using the Boltzmann approximation and certain other restrictions, N_i can be approximated by a multi-scale expansion,[17,18,22,23]

$$\begin{aligned} N_i = \frac{m_i \rho_l}{24}\{1 + 2\mathbf{c_i}\mathbf{u} + 3\mathbf{c_i}\mathbf{c_i} : \mathbf{uu} - \frac{3}{2} tr (\mathbf{uu}) \\ -6\nu_l \left[(\mathbf{c_i} \cdot \nabla) (\mathbf{c_i} \cdot \mathbf{u}) - \frac{1}{2} \nabla \cdot \mathbf{u} \right] + O \left(u^3, u \nabla u\right)\}. \end{aligned} \tag{12}$$

Using the approach similar to that introduced by Eggels and Somers,[18] the locally averaged mass conservation equation (Eq. (5)) is recovered by substituting Eq. (12) into Eq. (9), and carrying out the summation over all i with the first constraint in Eq. (10), the definitions in (11), and moments of N_i and Ω_i summarized in Appendix A 1,

$$\begin{aligned} \partial_t \sum_i N_i + \nabla \cdot \sum_i \mathbf{c_i} N_i = \sum_i \Omega_i (\mathbf{N}) , \\ \partial_t \rho_l + \nabla \cdot (\rho_l \mathbf{u}) = f^\phi. \end{aligned} \tag{13}$$

In a similar manner, by multiplying Eq. (9) by $\mathbf{c_i}$ and performing a summation over all i,

$$\begin{aligned} \partial_t \sum_i \mathbf{c_i} N_i + \nabla \cdot \sum_i \mathbf{c_i}\mathbf{c_i} N_i = \sum_i \mathbf{c_i}\Omega_i (\mathbf{N}) , \\ \partial_t (\rho_l \mathbf{u}) + \nabla \cdot (\rho_l \mathbf{uu}) = \nabla \cdot \sigma + \mathbf{f} + \mathbf{u} f^\phi, \end{aligned} \tag{14}$$

resulting in the locally averaged momentum conservation equations (Eq. (6)). Detailed discussions concerning the derivation of the collision operator and time evolution of the scheme are summarized in Appendix A 2.

B. Particle dynamics

The trajectories of individual particles can be tracked by various numerical methods depending on the level of physics being solved, e.g., the immersed boundary method,[26] the force-coupling model,[27] and the multiphase-particle-in-cell method.[28] Here, we are interested in a method that invokes a minimum set of physics required to capture the main features in sedimenting suspensions, yet economic for large amounts of particles and long simulation time. Therefore, the Lagrangian particle tracking (LPT) model with the distributed-point concept is chosen in this paper. In contrast to the point-particle concept in which particles do not occupy space in fluid, displacement of particles in fluid (i.e., the volume effect) is included in the distributed-particle concept. This results in the so-called three-way coupling which includes the effects of fluid on particle dynamics, the effects of particles on hydrodynamics, and the effects of the velocity disturbance in the fluid generated by other particles.[21] The first two effects are represented via the momentum coupling between phases. The latter is realized through the presence of the volume fraction in the conservation equations. Its

capability to reproduce particle dynamics has been proven by various authors[12,29–32] and will be further justified by favourable results obtained in this paper.

In the framework of the LPT model employed here, individual particles evolve in a time-dependent, three-dimensional manner under the influence of their properties and those of the fluid phase following Newton's equations of motion,

$$\partial_t \mathbf{x_p} = \mathbf{V}, \tag{15}$$

$$m_p \partial_t \mathbf{V} = \mathbf{F_N}, \tag{16}$$

with $\mathbf{x_p}$ the center position of the particle, $\mathbf{V}$ the particle velocity, and m_p the particle mass. The net force $\mathbf{F_N}$ acting on the particle is the sum of net gravity force $\mathbf{F_G}$, forces due to the stress gradients $\mathbf{F_S}$, drag force $\mathbf{F_D}$, net transverse lift force $\mathbf{F_L}$, and added mass force $\mathbf{F_A}$. The expressions for the forces above and their closures are provided in Appendix B 1. Note that the effects of the presence of other particles on the drag force are expressed as the product of the drag force on an unhindered particle and a hindrance function $g(\phi_p) = (1 - \phi_p)^{2.65}$ with ϕ_p the *local* particle volume fraction,[9] see Table I in Appendix B 1. The Basset history force $\mathbf{F_H}$ is neglected in this paper for physical and computational reasons. First, it is known that the effects of $\mathbf{F_H}$ are relatively small when the time-averaged quantities are of interest.[33] Second, the calculation of $\mathbf{F_H}$ requires significant amounts of computational resources. Neglecting $\mathbf{F_H}$ will not introduce large error and provide feasibility for simulations of large numbers of particles. Under the flow conditions considered in the present paper, preliminary tests showed that the rotational motion of the particles is insignificant for the simulation results. Hence, it is excluded from the LPT model. Since the ratio between the characteristic length of the flow field and the particle radius (ξ/r_p) used in this work is large compared to the particle size (see Fig. 2), it can be assumed that the Faxen forces, i.e., the term involving with $r_p^2 \bigtriangledown^2 \mathbf{u}$, are relatively small compared to other forces. Therefore, they are neglected in this work. This is justified by favorable results obtained in our work.

The particles affect the continuous fluid phase by exerting forces, and displacing the fluid. The momentum coupling is provided by the interphase forces (i.e., drag, lift, added mass, forces due to pressure, and stress gradients) acting on the fluid through the forcing term $\mathbf{F_p}$ in the momentum equation, Eq. (3). The displacement is described in terms of volume fraction ϕ_l in the continuity (Eq. (2)) and momentum equations (Eq. (3)). In this paper, we separate this effect in the form of the factor f^ϕ as shown in Sec. II A. The effect of f^ϕ will be determined and discussed in detail in Sec. III.

Since we restrict ourselves to dilute suspensions ($\phi_p \leq 0.01$) and finite particle Reynolds numbers (Re_p up to $O(10^0)$), particles will move smoothly (in the sense that the wake behind the particle[34] and the inertial effects are small[13]) with large interparticle separation $r_p \phi_p^{-1/3}$ compared to r_p. Therefore, the direct interactions (i.e., collisions between particles) are assumed to have negligible effects and are not considered.

In order to mathematically describe the coupling of quantities between Eulerian and Lagrangian reference frames, the mapping function with volume-weighted averaging is chosen.[35] A quantity Ψ_j on the Eulerian reference frame is mapped to the Lagrangian reference frame, and vice versa, by

$$\Psi_p = \frac{1}{V_l} \sum_{\forall j \in cell} \zeta_{cell}^j \Psi_j, \tag{17}$$

where Ψ_p is the quantity on the Lagrangian reference frame, and ζ_{cell}^j is the weighting function of the neighbor cells. In the framework of this paper, the fluid velocity $\mathbf{u}$, the fluid vorticity $\bigtriangledown \times \mathbf{u}$ at the center of the particle, and the particle volume fraction ϕ_p are transferred between the reference frames. Since the particle diameter d_p is small compared to the fluid's grid spacing h, the particles are assumed to interact only with fluid nodes in their immediate environment, i.e., 8 surrounding nodes in 3D space. Hence, the weighted function ζ_{cell}^j is described by

$$\zeta_{cell}^j = \left(h - |x_j - x_p|\right)\left(h - |y_j - y_p|\right)\left(h - |z_j - z_p|\right). \tag{18}$$

The subscripts p and j indicate the quantities on the Lagrangian and Eulerian reference frames, respectively. The choice of the d_p/h ratios of 0.1 and 0.25 employed in this work is a compromise

between a sufficiently fine grid resolution to capture fluid flow details and a sufficiently coarse grid resolution to keep the local averaging and distributed-particle approaches valid.

III. RESULTS AND DISCUSSION

In this section, we first discuss the numerical implementation. As mentioned earlier, we avoid complexities which may arise from the presence of walls and stratification of the particle concentration by considering only systems with monodisperse particles in a cubic periodic domain which are statistically uniformly distributed, see Fig. 1. The continuous fluid phase is discretized into a uniform cubic grid. The conservation equations of the fluid phase are solved using the extended lattice-Boltzmann scheme. Trajectories of individual particles are tracked in the framework of a Lagrangian particle tracking model with the distributed-point particle approach. Once a particle leaves through a boundary, it will appear at the opposite boundary.

The particle to fluid density ratio ρ_p/ρ_l is kept constant at 2.5 in all simulations except two sets of simulations in Sec. III C. The ratio between the domain size L and the particle diameter ($d_p = 2r_p$) is varied between 40 and 280. Grid resolution is varied by using the ratio between d_p and the grid space h of 0.1 and 0.25. The number of particles being tracked simultaneously is up to 470 000. The simulations start with quiescent fluid and particles at rest. The time increment in the simulations is chosen such that one Stokes time τ_s (i.e., the period required for a particle to travel over the distance of its radius r_p at its terminal velocity V_t) is discretized by 1000 time steps. A body force equal to the excessive weight due to particles $\mathbf{F_x} = (\bar{\rho}_d - \rho_l)\mathbf{g}$, with $\bar{\rho}_d$ the domain-average mixture density, is distributed uniformly throughout the fluid grid nodes to prevent an unbounded acceleration due to the periodic nature of the domain and the absence of solid walls. Hence, the particle velocity in the direction of gravity $V_\parallel$ in the simulations is the velocity relative to the reference frame moving with the fluid velocity induced by $\mathbf{F_x}$. Therefore, $V_\parallel$ is equivalent to the particle velocity observed in sedimentation experiments. The particle Reynolds number Re_p is varied in the range between 0.02 and 2.53 by varying the fluid viscosity ν_l. The simulations are typically carried out for 5000 Stokes times. The long-term average values presented in Secs. III A–III F are the values averaged over the last 2500 Stokes times where the simulations are in (quasi) steady state. The standard error of the mean $\sigma_M = \sigma/\sqrt{N_{mean}}$, measured with the standard deviation σ and the number of mean values N_{mean}, of the simulations is much smaller than the size of symbols we present in our graphs and error bars are omitted. Note that the mean values are taken every $5\tau_s$. Therefore, each mean value is sampled from an independent realization. All simulation results are shown in dimensionless form such that comparisons with available literature data can be performed conveniently. We present and discuss our simulation results for sedimenting suspensions at finite Re_p in the light of the understandings obtained from sedimentation experiments at low Re_p.[1–7,10,11,16,36–39]

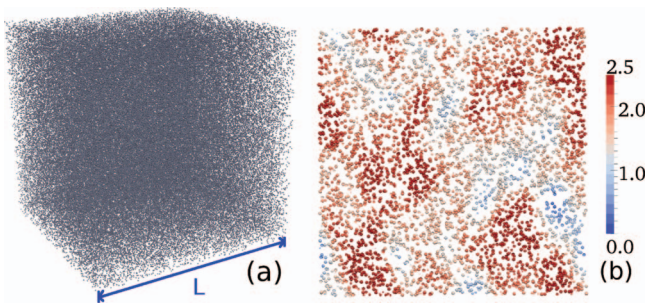

FIG. 1. Three-dimensional impression of the particles formation typically found in the simulations (a) and a cross section at the middle of the domain with the thickness of one grid node (b). The particles in (b) are colored by their velocity magnitude normalized by the terminal velocity $|\mathbf{V}|/V_t$ and enlarged 2.5 times its diameter for visualization purpose. The snapshot was taken at $t = 1000\tau_s$. The particles are randomly distributed in a cubic periodic domain with $Re_p = 0.05$, $\phi_p = 0.01$, $L/d_p = 200$, and $d_p/h = 0.25$. The total number of particles is 150 000.

A. Sedimenting suspension of spherical particles

First, we demonstrate the idea that a simulation with a set of closure relations (Appendix B 1) and a large number of particles results in complex behavior as observed in sedimentation experiments. Preliminary tests were carried out with a single particle sedimenting in a cubic periodic domain. As one would expect, the particle accelerates from rest to its terminal velocity V_t. We then carried out simulations of sedimenting suspensions in a cubic periodic domain with randomly, statistically uniformly distributed particles. An impression of a simulation with 150 000 particles is shown in Fig. 1(a). A cross-sectioned impression at the middle of the domain from a simulation with $Re_p = 0.05$ and $\phi_p = 0.01$ is shown in Fig. 1(b). Variations of the particle velocity magnitude $|\mathbf{V}|$ can be directly noticed. It can be further observed in the animation of the simulation that $|\mathbf{V}|$ slowly evolves with time. The animation is available upon request. The particle settling velocity vector field scaled by its terminal velocity mapped on an Eulerian grid for simulations with $Re_p = 0.05$ and 0.33 is shown in Figs. 2(a) and 2(b), respectively. The particle velocity fluctuations around the average, defined by $\delta\mathbf{V} = \mathbf{V} - \langle\mathbf{V}\rangle$, scaled by the average particle settling velocity in the direction parallel to gravity $\langle V_\parallel\rangle$ are shown in Figs. 2(c) and 2(d) for the simulations with $Re_p = 0.05$ and 0.33,

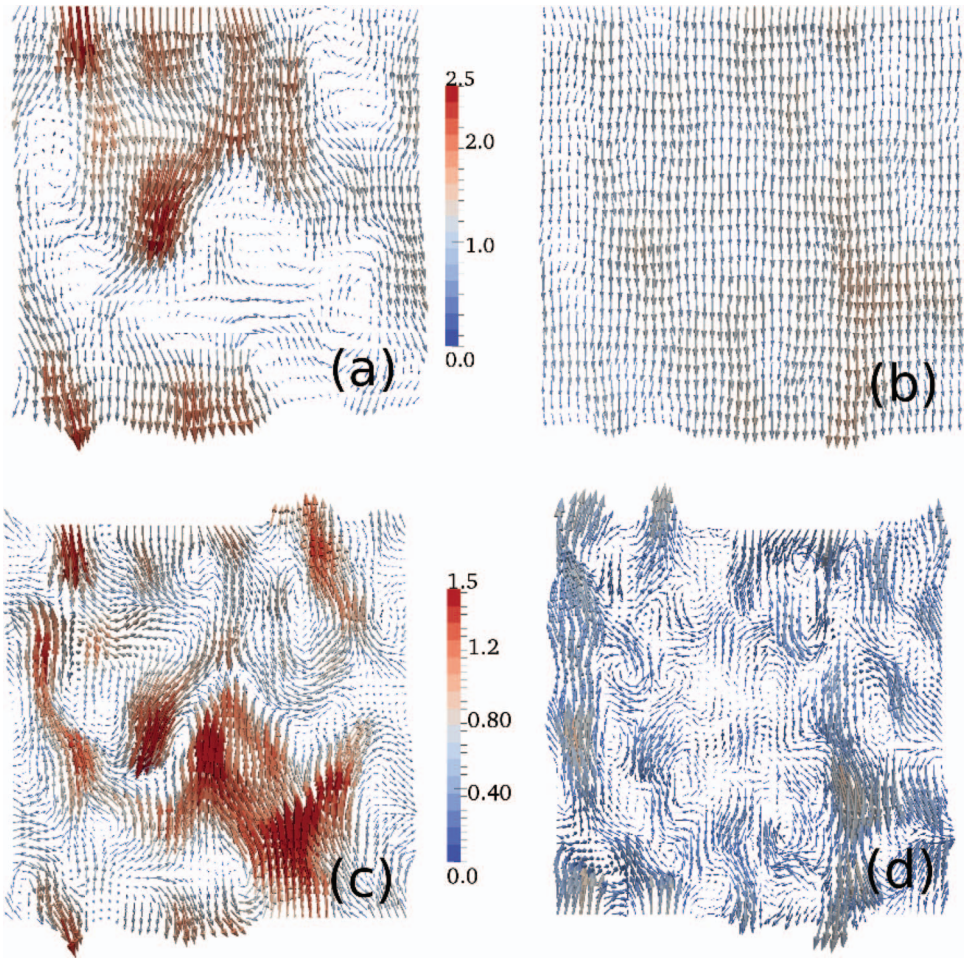

FIG. 2. Instantaneous particle velocity vector field $\mathbf{V}$ at the middle of the domain from the simulations with $Re_p = 0.05$ (a), and $Re_p = 0.33$ (b) scaled by the terminal velocity V_t according to the color scale. Instantaneous particle velocity fluctuations field $\delta\mathbf{V}$ from the simulation with $Re_p = 0.05$ (c), and $Re_p = 0.33$ (d) scaled by the average particle velocity in the direction parallel to gravity $\langle V_\parallel\rangle$ according to the color scale. The vector in (d) is magnified by a factor of 2 for visualization purpose. All instantaneous fields were taken at 4000 Stokes times. Both simulations are carried out with $\phi_p = 0.01$, $L/d_p = 200$, and $d_p/h = 0.25$.

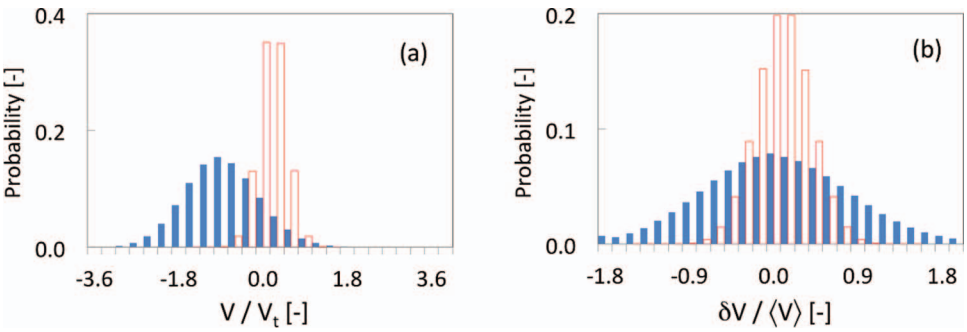

FIG. 3. Histogram of the long-term average particle velocity in the direction parallel (filled bars) and perpendicular (empty bars) to gravity (a), and the particle velocity fluctuations ratio (b). The simulation is carried out with $\phi_p = 0.01$, $Re_p = 0.05$, $L/d_p = 200$, and $d_p/h = 0.25$.

respectively. Despite the low Re_p values invoked in the simulations, the velocity fluctuations fields manifest high complexity, such as swirls, helical structures, and saddle points. These are reminiscent to the experimental data of Segre *et al.*[2] and Bernard-Michel *et al.*[37]

The long-term average velocity distributions in both directions are found to be smooth and have Gaussian shape, see Fig. 3(a). The mean value of the histogram of $\langle V_\parallel \rangle$ is higher than -1 indicating the hindrance effect due to hydrodynamic interactions, the effect from the particle displacement, and the buoyancy. The mean value of the average particle velocity in the direction perpendicular to gravity $\langle V_\perp \rangle$ is around zero. By subtracting the average values from the velocity histograms, the velocity fluctuations $\delta \mathbf{V}$ histogram in both directions can be compared directly. The distribution of the fluctuations around their means in Fig. 3(b) shows a larger variance of the fluctuations in the direction parallel to gravity. As a result, the amplitude of the fluctuations $\langle \Delta V_{\parallel,\perp} \rangle = \langle [V_{\parallel,\perp} - \langle V_{\parallel,\perp} \rangle]^2 \rangle^{1/2}$ is found to be highly anisotropic with higher magnitude in the direction parallel to gravity. These behaviors are in accordance with the experimental observations reported by various authors.[2,6,37,40]

The average particle velocity in the direction parallel to gravity $\langle V_\parallel \rangle$ and the fluctuation amplitudes $\langle \Delta V_{\parallel,\perp} \rangle$ slowly evolve with time to their (quasi) steady values. In sedimenting suspensions, particles initially cause perturbation in the fluid which accelerates particles around $t/\tau_s = 35$, then the velocity drops to its steady value, see Fig. 4(a). Following the same trend, large particle velocity fluctuations were initially developed, reached a peak value around $t/\tau_s = 180$, and slowly decayed to its steady level, see Fig. 4(b). Similar behavior is also observed experimentally (at low Re_p)[36] and numerically (at finite Re_p).[16] However, quantitative comparison of the initial velocity fluctuations to the experimental data cannot be done. This is because the flow conditions in experiments are complicated by the presence of walls, stratification, and the initial mixing of the suspensions. Furthermore, several authors believe that the evolution of the microstructure in sedimenting suspensions could be

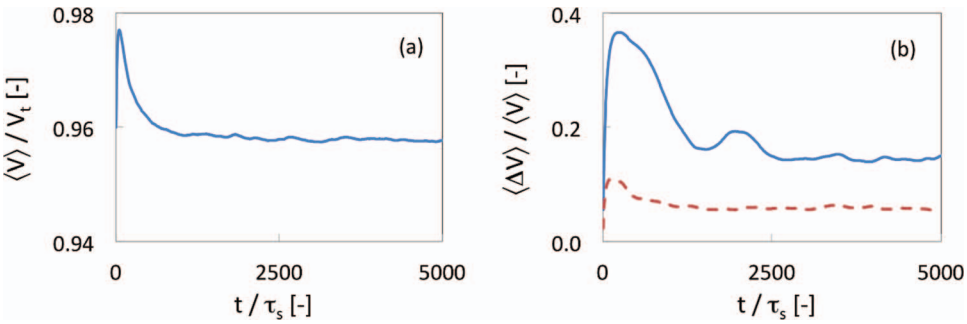

FIG. 4. Development of the average particle settling velocity ratio $\langle V_\parallel \rangle / V_t$ in the direction parallel to gravity (a) and the average fluctuation amplitudes ratio $\langle \Delta V_{\parallel,\perp} \rangle / \langle V_\parallel \rangle$ (b) in the direction parallel (solid line) and perpendicular (dashed line) to gravity. The simulation is carried out with $\phi_p = 0.01$, $Re_p = 0.52$, $L/d_p = 200$, and $d_p/h = 0.25$.

used to explain the so-called screening mechanism of fluctuation amplitudes, i.e., the independent of particle velocity fluctuations from the domain size. Several ideas related to the microstructure and the screening mechanism have been proposed in the literature, such as three-body hydrodynamic interactions,[41] convection of density fluctuations,[14] the effects of vertical walls,[39] and the effects of horizontal walls.[42] No conclusion has been drawn. The evolution of the fluctuation amplitudes and microstructure in sedimenting suspensions is subjected to our future work. Additional information can be found in literature.[6,16,43]

Note that, in our preliminary tests, the effect of initial particle position is found to be insignificant when the particles are statistically uniformly distributed. This is mainly due to large numbers of particles and long simulation times used in the present work. In order to avoid the uncertainty at the initial phase of the sedimentation, only the long-term average values in the period between $t/\tau_s = 2500$ and 5000 are used in the present paper.

B. Particle volume fraction effects

It is well known that the average particle velocity in the direction parallel to gravity $\langle V_\parallel \rangle$ is lower than the terminal velocity V_t.[7–9] The hindrance effect is taken into account explicitly via the hindrance function $g(\phi_p)$ (see Table I in Appendix B 1) and implicitly through the fluid volume fraction $\phi_l = 1 - \phi_p$ in the conservation equations of the fluid phase. Our simulations are able to capture the hindrance in $\langle V_\parallel \rangle$ as a function of ϕ_p with deviations from the Richardson-Zaki correlation (Eq. (1) with $k = 1$, and $n = 4.65$) less than 1%, see Fig. 5. The results are independent from the d_p/h ratios used in the simulations. This implies that the Richardson-Zaki correlation exponent $n = 4.65$ contains contributions from the hindrance effect due to hydrodynamic interactions (with the exponent 2.65 in the hindrance function), the effect from the particle displacement, and the buoyancy.

In a sedimenting suspension within a sufficiently large domain size at low Re_p, the fluctuation amplitudes were found experimentally to depend solely on ϕ_p and scaled with $\phi_p^{1/3}$ as[2,6]

$$\left\langle \Delta V_{\parallel,\perp} \right\rangle = C_{1,(\parallel,\perp)} \phi_p^{1/3}. \tag{19}$$

The experimental data were found to be well fitted with the values of the fluctuation amplitudes scaling constants $C_{1,\parallel}$ in the range between 2 and 3, and $C_{1,\perp}$ in the range between 1 and 1.5.[6,43] At $Re_p = 0.05$, the simulated $\langle \Delta V_\parallel \rangle$ and $\langle \Delta V_\perp \rangle$ values resemble the scaling observed in experiments at low Re_p with $C_{1,\parallel} = 3$, and $C_{1,\perp} = 1$, respectively, see Fig. 6(a). This agreement with experimental observations is used to validate the ability to correctly predict the second-order statistics (i.e., the velocity variance) of the present numerical method. Noticeably, at $Re_p = 0.33$, the simulated $\langle \Delta V_\parallel \rangle$ and $\langle \Delta V_\perp \rangle$ values are well below the scaling derived from the experiments at low Re_p (Eq. (19)), see Fig. 6(b). However, this result is in accordance with the recent finding of Yin and Koch[16] that the fluctuation amplitudes decrease with increasing Re_p at sufficiently high Re_p. This suggests that, between the Re_p values of 0.05 and 0.33, additional physics which are unimportant at low Re_p begin

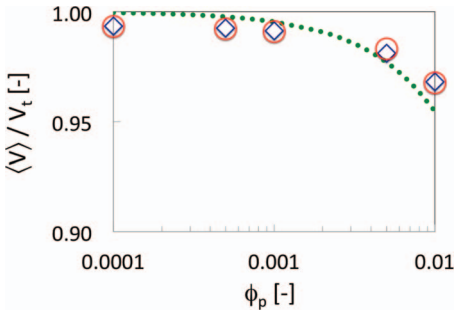

FIG. 5. Long-term average particle settling velocity ratio $\langle V_\parallel \rangle / V_t$ in the direction parallel to gravity versus particle volume fraction ϕ_p from the simulation with $Re_p = 0.05$ (circles) and $Re_p = 0.33$ (diamonds). The dotted line is the prediction from Richardson-Zaki correlation (Eq. (1)) with $n = 4.65$ and $k = 1.0$.

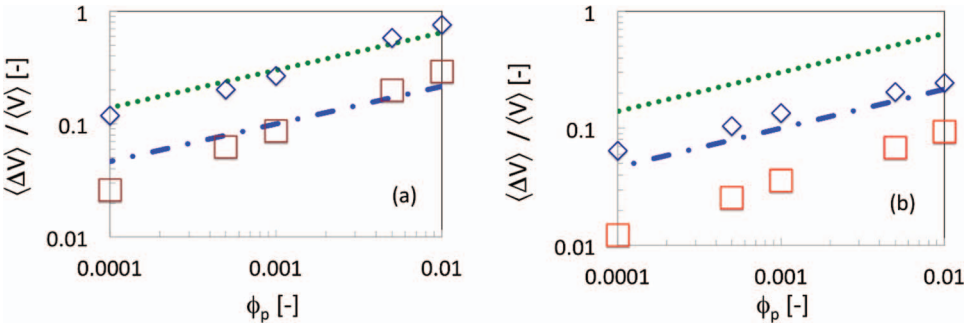

FIG. 6. Long-term average fluctuation amplitudes ratio $\langle \Delta V_{\parallel,\perp} \rangle / \langle V_{\parallel} \rangle$ in the directions parallel (diamonds) and perpendicular (squares) to gravity versus particle void fraction ϕ_p with $Re_p = 0.05$ (a) and $Re_p = 0.33$ (b). Dotted and dotted-dashed lines are the calculations from $\langle \Delta V_{\parallel} \rangle / \langle V_{\parallel} \rangle = 3\phi_p^{1/3}$ and $\langle \Delta V_{\perp} \rangle / \langle V_{\parallel} \rangle = \phi_p^{1/3}$, respectively.

to characterize the suspension leading to the dependence of the scaling of $\langle \Delta V_{\parallel,\perp} \rangle$ on Re_p. This observation will be further discussed in Sec. III C.

C. Particle Reynolds number Re_p effects

In a sedimenting suspension, the complexity in hydrodynamics is initially induced by the random nature of the suspension microstructure, i.e., the distribution of the particle positions. The hydrodynamics, in turn, determine the complexity in the particle dynamics. Following the study of Re_p effects by Yin and Koch,[16] Re_p is varied while the particle to fluid density ratio ρ_p/ρ_f is kept constant. This setting mimics possible experiments where Re_p is varied by changing the fluid viscosity with the same set of particles. Figure 7 shows simulated fluctuation amplitudes $\langle \Delta V_{\parallel,\perp} \rangle$ as a function of Re_p for $\phi_p = 0.01$ and 0.005. At low Re_p, $\langle \Delta V_{\parallel,\perp} \rangle$ depend only weakly on Re_p and are known to reach a constant $\langle \Delta V \rangle / \langle V \rangle$ at very low Re_p.[6] When Re_p is increased beyond a certain value, $\langle \Delta V_{\parallel,\perp} \rangle$ decrease with increasing Re_p. The transition in the scaling behavior occurs at a critical particle Reynolds number $Re_{p,c}$ beyond which $\langle \Delta V_{\parallel,\perp} \rangle$ start to depend on Re_p. Our simulation results for both $\phi_p = 0.01$ and 0.005 suggest $Re_{p,c} \approx 0.08$. This value agrees well with $Re_{p,c} = 0.1$ proposed by Yin and Koch.[16] The values of $\langle \Delta V_{\parallel} \rangle$ and $\langle \Delta V_{\perp} \rangle$ at Re_p below $Re_{p,c}$ agree fairly well with Eq. (19) with $C_{1,\parallel} = 3$ and $C_{1,\perp} = 1$, respectively. Furthermore, the simulation results exhibit only weak dependence on the choice of d_p/h ratio, which can be directly observed in Fig. 7: simulation results from different d_p/h ratios follow similar trends in $\langle \Delta V_{\parallel,\perp} \rangle$. This indicates that the results are independent of the spatial resolution.

As mentioned above, Re_p in the simulations set shown in Fig. 7 is varied by changing the fluid viscosity while ρ_p/ρ_f is kept constant. Consequently, the Stokes number, given by $St = \tau_p/\tau_l$

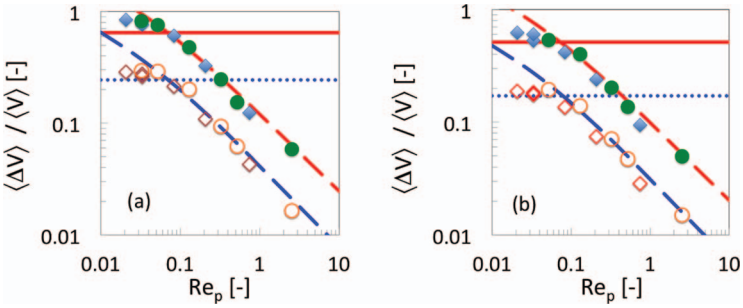

FIG. 7. Long-term average fluctuation amplitudes ratio as a function of the particle Reynolds number Re_p in the direction parallel (filled symbols) and perpendicular (empty symbols) to gravity with $d_p/h = 0.1$ (diamonds), and $d_p/h = 0.25$ (circles). Simulations are carried out with $\phi_p = 0.01$ (a), and $\phi_p = 0.005$ (b). The solid and dotted lines are the calculations from $\langle \Delta V_{\parallel} \rangle / \langle V_{\parallel} \rangle = 3\phi_p^{1/3}$, and $\langle \Delta V_{\perp} \rangle / \langle V_{\parallel} \rangle = \phi_p^{1/3}$, respectively. The dashed lines are the prediction using Eq. (20).

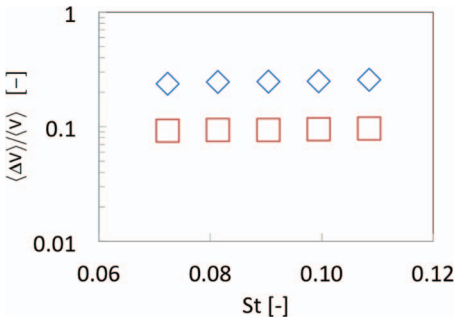

FIG. 8. Long-term average fluctuation amplitudes ratio as a function of the Stokes number in the direction parallel (diamond symbols) and perpendicular (square symbols) to gravity with $d_p/h = 0.25$, $\phi_p = 0.01$, $L/d_p = 200$, and $Re_p = 0.33$.

where τ_p is the characteristic time of dynamic relaxation for the particles and τ_l is a time characteristic of the fluid flow field,[21,44] varies with Re_p. Within the parameter ranges considered here, $St = \rho_p Re_p/(9\rho_f)$. In order to separate the effects of St from Re_p, two additional sets of simulations have been carried out. In the first set, Re_p is kept constant at 0.33 while St is varied in the range between 0.07 and 0.11 by varying the fluid viscosity and ρ_p/ρ_f between 2 and 4. It can be directly observed from Fig. 8 that, in the range studied here, St has no significant effect on $\langle \Delta V_{\parallel,\perp} \rangle$. In the second set, Re_p is varied while St is kept constant at 0.09. The dependency of $\langle \Delta V_{\parallel,\perp} \rangle$ on Re_p closely follows the trend found in the previous set of simulations where Re_p was varied while ρ_p/ρ_f was kept constant, see Fig. 9. Based on these results, it can be concluded that $\langle \Delta V_{\parallel,\perp} \rangle$ are determined mainly by the agitation of the fluid phase by the particles (i.e., the Re_p effects), while the level of response between particles and fluid phase, i.e., St number, has no significant effect. Hence, the transition of the scaling behavior found in Fig. 7 might stem from the instability in the fluid flow field, e.g., brakeup of fluid vortices, occurring beyond $Re_{p,c} \sim 0.08$ (corresponding to $St \sim 0.02$). A detailed study of liquid flow field and its effect on the scaling of $\langle \Delta V_{\parallel,\perp} \rangle$ is the subject of our future work.

At (quasi) steady state and a sufficiently large domain size, a suspension contains swirl structures of various sizes and velocity magnitudes. The length over which the particle dynamics are correlated, i.e., the correlation length ξ, can be determined through the spatial correlation function of $\langle \Delta V_{\parallel} \rangle$ along the direction perpendicular to gravity. The location where the spatial correlation function gets zero provides an estimate of ξ.[36] The magnitude of ξ is a measure for the average size of the swirl structures in the suspension. In the low Re_p regime, ξ was found experimentally to be approximately 20 times the interparticle separation $r_p \phi_p^{1/3}$, and independent from Re_p.[2,6,36] A comparison of the long-term average correlation functions of $\langle \Delta V_{\parallel} \rangle$ along the direction perpendicular to gravity from the simulations with Re_p in the range between 0.03 and 0.52 (Fig. 10) demonstrates a decrease in

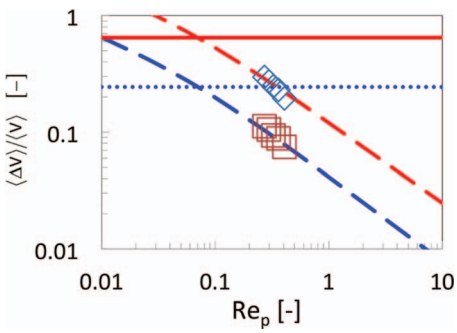

FIG. 9. Long-term average fluctuation amplitudes ratio as a function of the particle Reynolds number Re_p in the direction parallel (diamond symbols) and perpendicular (square symbols) to gravity with $d_p/h = 0.25$, $\phi_p = 0.01$, $L/d_p = 200$, and $St = 0.09$. The solid and dotted lines are the calculations from $\langle \Delta V_{\parallel} \rangle / \langle V_{\parallel} \rangle = 3\phi_p^{1/3}$, and $\langle \Delta V_{\perp} \rangle / \langle V_{\parallel} \rangle = \phi_p^{1/3}$, respectively. The dashed lines are the prediction using Eq. (20).

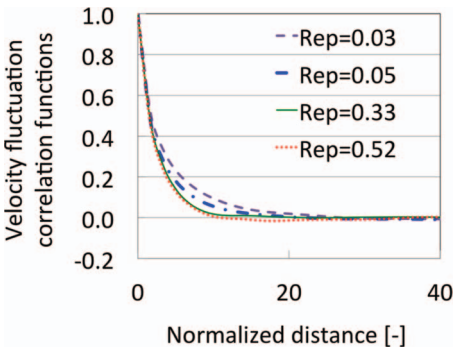

FIG. 10. Long-time average spatial correlation functions of the particle velocity fluctuation in the direction parallel to gravity $\langle V_{\parallel} \rangle$ along the direction perpendicular to gravity versus distance normalized by the interparticle separation $x/r_p\phi_p^{-1/3}$ at various Reynolds numbers. The simulation is carried out with $\phi_p = 0.01$, $L/d_p = 200$, and $d_p/h = 0.25$.

ξ with increasing Re_p. A similar trend has been reported in the numerical simulations of Climent and Maxey.[27] We depict the finding by showing the particle velocity field around the average $\delta\mathbf{V} = \mathbf{V} - \langle \mathbf{V} \rangle$ at $Re_p = 0.05$ and 0.33 in Figs. 2(c) and 2(d), respectively. Smaller swirl structures can be noticed from the simulation result with $Re_p = 0.33$. These results suggest that, in the finite Re_p regime, $\langle \Delta V_{\parallel,\perp} \rangle$ and ξ decrease with increasing Re_p.

D. Domain size effects

Consider a situation, in which the domain size L is only a few times larger than the interparticle separation $r_p\phi_p^{-1/3}$. The swirls will then have a size of the order of the domain size. If L is further enlarged by a few interparticle separations, while the particle volume fraction ϕ_p and the particle Reynolds number Re_p are kept constant, the swirl sizes will also increase. As a result, the fluctuation amplitudes $\langle \Delta V_{\parallel,\perp} \rangle$ increase following the swirl sizes. However, when L is larger than a characteristic swirl size L_s, the swirl sizes will not increase with L. Consequently, $\langle \Delta V_{\parallel,\perp} \rangle$ get saturated and independent from L. Here, L_s is defined as the length in which $\langle \Delta V_{\parallel,\perp} \rangle$ are within a 10% range of their magnitude when they are independent from L. This behavior has been demonstrated experimentally by Segre *et al.*[2] at $Re_p \sim O(10^{-3})$. Similar behavior exists in sedimenting suspensions at finite Re_p. We demonstrate this by carrying out simulations of sedimenting suspensions at $Re_p = 0.33$ and $\phi_p = 0.01$ with varying domain size L in the range between 17 to 120 times the interparticle separation $r_p\phi_p^{-1/3}$. The fluctuation amplitudes $\langle \Delta V_{\parallel,\perp} \rangle$ as a function of L are plotted in Fig. 11(a). It can be observed that $\langle \Delta V_{\parallel,\perp} \rangle$ increase with L. The characteristic swirl size L_s in the suspensions with $Re_p = 0.33$ and $\phi_p = 0.01$ is $\sim 50\, r_p\phi_p^{-1/3}$. In a similar manner, the simulations with $Re_p = 0.05$ and $\phi_p = 0.01$ (Fig. 11(b)) indicate L_s around $110\, r_p\phi_p^{-1/3}$. These results show that L_s decreases with increasing Re_p, and $\langle \Delta V_{\parallel,\perp} \rangle$ get saturated at a smaller $L/(r_p\phi_p^{-1/3})$ ratio when Re_p increases. We further investigate the dependency of fluctuation amplitudes by carrying out simulations with particle volume fractions of 0.01, 0.005, and 0.001. The simulation results are shown in Figs. 11(a), 11(c), and 11(d), respectively. The values of L_s are around 50, 45, and 25 times the interparticle separation as the particle volume fraction decreases. These results suggest that $\langle \Delta V_{\parallel,\perp} \rangle >$ get saturated at a smaller $L/(r_p\phi_p^{-1/3})$ ratio when ϕ_p decreases.

E. Analysis of sedimenting suspensions at finite Re_p

In light of the results obtained from our simulations, the behavior of sedimenting suspensions at finite-particle Reynolds numbers has been revealed. In such system, the complex hydrodynamics are induced by the random nature of the suspension microstructure, i.e., the distribution of the particle positions. The hydrodynamics, in return, cause the complexities in the particle dynamics via hydrodynamic interactions. Consequently, these interactions form swirls which contain a large

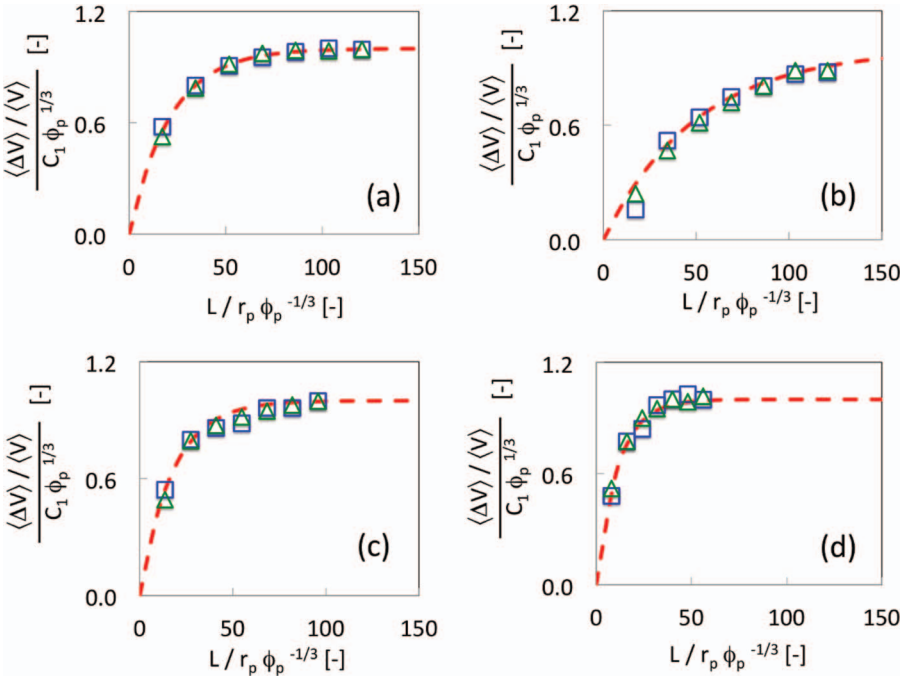

FIG. 11. Long-term average fluctuation amplitudes $\langle \Delta V_{\parallel,\perp} \rangle / \langle V_{\parallel} \rangle$ in the direction parallel (squares) and perpendicular (triangles) to gravity normalized by $C_{1,(\parallel,\perp)}\phi_p^{1/3}$ versus the normalized domain size $L/r_p\phi_p^{-1/3}$. All simulations have $d_p/h = 0.25$ with $\phi_p = 0.01$ and $Re_p = 0.33$ (a), $\phi_p = 0.01$ and $Re_p = 0.05$ (b), $\phi_p = 0.005$ and $Re_p = 0.33$ (c), and $\phi_p = 0.001$ and $Re_p = 0.33$ (d). Dotted lines are the fit using Eq. (20). The values of $C_{1,\parallel}$ in the case (a), (b), (c), and (d) are equal to 1.20, 4.37, 1.24, and 1.35, respectively. The values of C_2 in the case (a), (b), (c), and (d) are equal to 21.23, 50.00, 17.58, and 11.34, respectively.

number of particles. After a sufficiently long time, effects of initial conditions vanish and swirls constantly are generated and destroyed in the suspension. The fluctuation amplitudes $\langle \Delta V_{\parallel,\perp} \rangle$ related to $\langle V \rangle$ and the correlation length ξ decrease with increasing Re_p (see Sec. III C). Furthermore, it is found that $\langle \Delta V_{\parallel,\perp} \rangle$ get saturated at a smaller $L/(r_p\phi_p^{-1/3})$ ratio with increasing Re_p and decreasing ϕ_p (see Sec. III D).

In order to express these relations mathematically, we extended the correlation derived from the sedimentation experiments at low Re_p by Segre *et al.*[2] for sedimenting suspensions at Re_p greater than $Re_{p,c} \sim 0.08$. From earlier discussion, it follows that the scaling of $\langle \Delta V_{\parallel,\perp} \rangle$ is a function of ϕ_p, Re_p, and L. Therefore, the fluctuation amplitude scaling constants $C_{1,(\parallel,\perp)}$ and characteristic length scaling constant C_2 as proposed by Segre *et al.*[2] are replaced by functions $C_{1,(\parallel,\perp)}(Re_p, \phi_p)$ and $C_2(Re_p, \phi_p)$, respectively. The new correlation has the form

$$\frac{\langle \Delta V_{\parallel,\perp} \rangle}{V_{\parallel}} = C_{1,(\parallel,\perp)}\left(Re_p, \phi_p\right)\phi_p^{1/3}\left[1 - \exp\left(\frac{-L}{C_2\left(Re_p, \phi_p\right) r_p \phi_p^{-1/3}}\right)\right]. \tag{20}$$

It is assumed that the functions $C_{1,(\parallel,\perp)}(Re_p, \phi_p)$ and $C_2(Re_p, \phi_p)$ are power functions of the form $a Re_p^b \phi_p^c$ with fitting parameters a, b, and c. The values of each parameter are determined using the simulation sets described in Sec. III D which are carried out with various Re_p, ϕ_p, and L (Fig. 11). The total number of simulations is 28 with two data points ($\langle \Delta V_{\parallel} \rangle$ and $\langle \Delta V_{\perp} \rangle$) per simulation. First, we consider only the fluctuation amplitude in the direction parallel to gravity $\langle \Delta V_{\parallel} \rangle$. In each simulation set, the values of the functions $C_{1,\parallel}(Re_p, \phi_p)$ and $C_2(Re_p, \phi_p)$ which provide the best fit to the simulation results are determined. Then, the fitting parameters a, b, and c for the function $C_{1,\parallel}(Re_p, \phi_p)$ and $C_2(Re_p, \phi_p)$ are estimated. The process is repeated iteratively until the functions $C_{1,\parallel}(Re_p, \phi_p)$ and $C_2(Re_p, \phi_p)$ provide best fit for all simulation sets.

It is known that, at low Re_p, the fluctuation amplitude in the direction parallel and perpendicular to gravity relate with each other with an anisotropy ratio $\gamma_a = C_{1,\parallel}/C_{1,\perp}$ in a range between 2 and 4.[2,6] We assume that the fluctuation amplitudes also relate in the same way at finite Re_p. We further assume that γ_a depends on Re_p and ϕ_p with the form of power function similar to the expression of the function $C_{1,\parallel}(Re_p, \phi_p)$ with a different set of fitting parameters. The iterative procedure described above is used to determine the values of the fitting parameters.

The fluctuation amplitude scaling function is found to be

$$C_{1,\parallel}\left(Re_p, \phi_p\right) = 0.44 Re_p^{-0.69} \phi_p^{-0.05}. \tag{21}$$

When the domain size L is sufficiently large, the domain size effect is negligibly small (i.e., the square bracket in Eq. (20) is approximately unity). Equation (20) becomes

$$\frac{\langle \Delta V_\parallel \rangle}{V_\parallel} = 0.44 Re_p^{-0.69} \phi_p^{0.28}. \tag{22}$$

It can be implied from Eq. (22) that $\langle \Delta V_\parallel \rangle$ decreases with increasing Re_p. This is in accordance with the discussion concerning the effect of Re_p in Sec. III C. It is important to note that, below the critical particle Reynolds number $Re_{p,c}$, the fluctuation amplitudes scale with ϕ_p with an exponent of 0.33. This is in accordance with the exponent found in the experiments by Segre *et al.*[2] Beyond $Re_{p,c}$, the exponent is slightly modified by the fluctuation amplitude scaling function to a value of 0.28. Yin and Koch[16] found that the fluctuation amplitudes scale with Re_p with an exponent of -1. It can be argued that in their work, the exponent was extracted from simulations at Re_p higher than approximately 3 which is greater than the maximum Re_p considered here. Noticeably, their simulation results at lower Re_p exhibit Re_p dependency with a higher exponent (i.e., less negative). Hinch[14] and Guazzelli and Hinch[6] estimate the dependency of the fluctuation amplitudes on Re_p with an exponent of $-1/3$ based on the Poisson estimation with the blob concept. Our simulations suggest an exponent of approximately $-2/3$. The anisotropy of the fluctuation amplitudes is expressed as

$$\gamma_a = 1.66 Re_p^{0.04} \phi_p^{-0.12}. \tag{23}$$

The expression above implies that the anisotropy only very weakly depends on Re_p and decreases with increasing ϕ_p. At higher ϕ_p, the interparticle separation is smaller. Hence, the hydrodynamic interactions are stronger resulting in a weaker anisotropy.

The characteristic length scaling function is expressed as

$$C_2(Re_p, \phi_p) = 45 Re_p^{-0.45} \phi_p^{0.27}. \tag{24}$$

With a constant value of the fluctuation amplitude scaling factors (the multiplication factor of the square bracket on the right-hand side), Eq. (20) describes the dependency of the fluctuation amplitudes on the domain size L. Following the discussion in Sec. III D, it can be noticed that the value of the square bracket converges to unity when L is larger than the characteristic swirl size L_s resulting in the independence of $\langle \Delta V_{\parallel,\perp} \rangle$ from L. By its definition, the magnitude of L_s is around 2.5 times $C_2(Re_p, \phi_p) r_p \phi_p^{-1/3}$.

We now examine the ability to represent the fluctuation amplitudes of the correlation proposed above (Eq. (20)) with other sets of simulations. It can be seen that the correlation correctly represents the scaling of the fluctuation amplitudes in dependency with the particle volume fraction at $Re_p = 0.33$, see Fig. 12(b). As expected, deviations occur at Re_p lower than $Re_{p,c}$, see Fig. 12(a). The dependence of the fluctuation amplitudes beyond $Re_{p,c}$ on Re_p is correctly represented by the correlation, see Figs. 7(a) and 7(b). Also, the correlation is able to represent the fluctuation amplitudes predicted by simulations with different d_p/h ratios supporting independency of the results from spatial resolution (see Fig. 7).

F. Particle displacement effects

Owing to the derivation of the conservation equations at high ϕ_p presented earlier (Eqs. (5) and (6)), the displacement of fluid by the particles is mimicked through the factor f^ϕ.

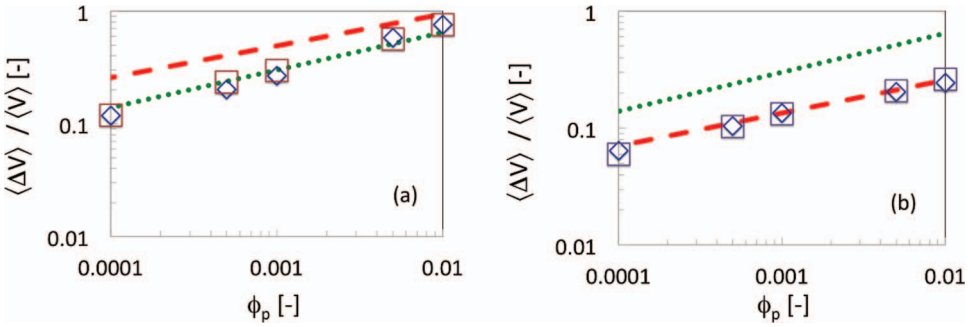

FIG. 12. Long-term average fluctuation amplitudes ratio $\langle \Delta V_{\parallel,\perp} \rangle / \langle V_{\parallel} \rangle$ in the directions parallel (diamonds) and perpendicular (squares) to gravity versus particle void fraction ϕ_p with $Re_p = 0.05$ (a) and $Re_p = 0.33$ (b). Perpendicular fluctuation amplitudes are scaled by the anisotropy ratio γ_a. Dotted and dashed lines are the prediction with $\langle \Delta V_{\parallel} \rangle / \langle V_{\parallel} \rangle = 3\phi_p^{1/3}$ and Eq. (20), respectively. The simulations are carried out with a sufficiently large domain size to avoid size-dependence effects.

The volume fraction also appears in the back-coupling force term $\mathbf{F_p}/(\phi_p V_l)$. In order to demonstrate the effect of the particle displacement, we carried out two sets of simulations at low to high ϕ_p; one with the volume fraction, and another without the volume fraction in the conservation equations. In order to be able to simulate dense particle systems without invoking particle collisions, the particles are arranged in a face-centered cubic formation, i.e., the distance from a particle to its surrounding neighbors is identical. Hence, the gradient and temporal variation of the volume fraction are zero, i.e., $f^{\phi} = 0$. The effect of the particle displacement is represented only in the back-coupling force term. Long-term average particle settling velocity in the direction parallel to gravity $\langle V_{\parallel} \rangle$ from both sets of simulations for various ϕ_p are shown in Fig. 13. At low ϕ_p (i.e., high liquid volume fraction $\phi_l = 1 - \phi_p$), $\langle V_{\parallel} \rangle$ from both sets is only marginally different. While, in the moderate ϕ_p regime, $\phi_p \sim 0.10$, $\langle V_{\parallel} \rangle$ from the simulations including volume fraction effects is significantly lower than the ones without volume fraction effect. This is due to the fact that the back-coupling force term has a higher magnitude in the simulations including volume fraction effects, which induces a higher magnitude of fluid flow against the particle motion. A quantitative difference in settling velocities is estimated by comparing the best fit correlation in a form similar to the Richardson-Zaki correlation. The liquid volume fraction in the back-coupling force term (the second term on the rhs of Eq. (6)) contributes to the exponent n with a magnitude of approximately 0.8. Note that, since the simulations are carried out with an *ideal* configuration of particles within an unbounded domain, this comparison should not be related to the settling velocity in a more *realistic* system with randomly distributed particles.

Next, the particles in both sets of simulations are generated randomly with a statistically uniform configuration. Hence, the effect of f^{ϕ} is included in the simulations with the volume fraction. We

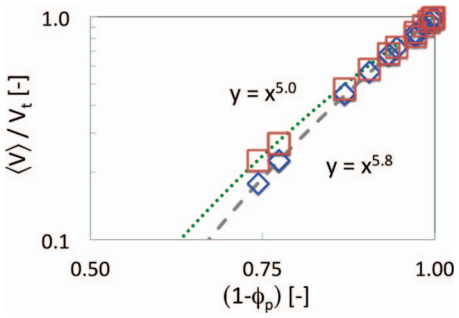

FIG. 13. Long-term average particle settling velocity ratio $\langle V_{\parallel} \rangle / V_t$ from simulations with ordered particles formation as a function of liquid volume fraction $(1 - \phi_p)$ for simulations with (diamonds) and without the factor f^{ϕ} (squares). Dotted and dashed lines, and the equations next to them represent best fits for the simulation with and without the factor f^{ϕ}, respectively. The simulations are carried out with $L/d_p = 200$, and $d_p/h = 0.25$.

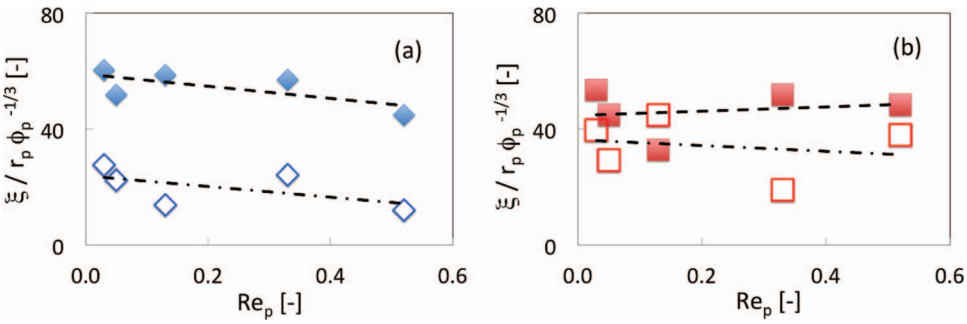

FIG. 14. Long-time average correlation length ξ normalized by the interparticle separation $r_p\phi_p^{-1/3}$ in the direction parallel (filled symbols) and perpendicular (empty symbols) to gravity from the simulations with (a) and without the volume fraction effect (b). The simulations are carried out with $\phi_p = 0.01$, $L/d_p = 200$, and $d_p/h = 0.25$. Lines represent trend using linear fitting method.

carried out simulations with ϕ_p up to 0.01. As expected, the mean settling velocity $\langle V_\parallel \rangle$ and the fluctuation amplitudes $\langle \Delta V_{\parallel,\perp} \rangle$ are not significantly different in both sets. However, differences between simulations with and without the liquid volume fraction are found if the particle Reynolds number Re_p is varied, see Fig. 14. In the simulations with volume fraction effects, the correlation length ξ decreases with increasing Re_p. The simulations without volume fraction effect provide no dependence between ξ and Re_p. This result suggests that the factor f^ϕ, which arose from the presence of the volume fraction in the conservation equations and contains the gradient of the volume fraction, relates to long-range hydrodynamic interactions between particles.

IV. SUMMARY AND CONCLUSION

We propose an alternative numerical method for simulations of sedimenting suspensions. Different from the approaches by Elgobashi[45,46] and Kuipers,[47,48] we use an extended lattice-Boltzmann scheme to discretize the locally averaged conservation equations. It offers a simple and computationally efficient way to perform large scale simulations of sedimenting suspensions. The extended lattice-Boltzmann scheme coupled with a Lagrangian particle tracking model is able to reproduce the main features of sedimenting suspensions, such as swirls, helical structures, and saddle points, in accordance with the experimental data available in the literature.[37] Within the low particle volume fraction ϕ_p regime considered in this paper, the simulated particle settling velocity $\langle V_\parallel \rangle$ agrees well with the Richardson-Zaki correlation (Eq. (1)).[8,9] Furthermore, at low Re_p, the simulated fluctuation amplitudes $\langle \Delta V_{\parallel,\perp} \rangle$ closely follow the scaling derived from the experimental data available in the literature (Eq. (19)).[2,6,43] These results confirm the ability to reproduce the first-order (i.e., the mean settling velocity) and second-order (i.e., the fluctuation amplitudes) statistics of the present numerical method.

At finite Re_p, our simulation results suggest a transition of scaling behavior of the fluctuation amplitudes $\langle \Delta V_{\parallel,\perp} \rangle$ at $Re_{p,c} = 0.08$. The value of $Re_{p,c}$ is in accordance with the value of $Re_{p,c}$ proposed by Yin and Koch[16] using a surface-resolved numerical simulation method. In contrast to previous simulations of sedimenting suspensions,[13,16,27] we are able to demonstrate that fluctuation amplitudes get independent of the domain size when sufficiently large domain size and simulation time are invoked. We found that, at finite Re_p, $\langle \Delta V_{\parallel,\perp} \rangle$ are functions of Re_p and ϕ_p. In the spirit of the correlation derived by Segre *et al.*,[2] we propose a correlation that correctly represents $\langle \Delta V_{\parallel,\perp} \rangle$ in terms of ϕ_p, Re_p, and L (Eq. (20)).

In conclusion, the present numerical method is able to reproduce complex behavior found in sedimenting suspensions within the dilute suspension limit. Mechanisms behind the behavior of sedimenting suspensions at finite Re_p are numerically demonstrated and discussed. Our findings are analyzed and formulated into a simple correlation.

ACKNOWLEDGMENTS

We acknowledge Western Canada Research Grid for computation facility. One of the authors (R.S.) would like to thank A. Komrakova for helpful discussion concerning the correlation functions.

APPENDIX A: DERIVATIONS OF THE EXTENDED LATTICE-BOLTZMANN SCHEME

1. Moments of the mass density and the collision operator

In this section, the definitions of the mass density N_i and the constraints of the collision operator Ω_i introduced earlier will be proven. The summation of the first few moments of N_i and Ω_i will be carried out over all velocity direction index i using the following symmetry properties of the FCHC lattice:

$$\begin{aligned}
\sum_i m_i &= 24,\\
\sum_i m_i c_{i\alpha} &= 0,\\
\sum_i m_i c_{i\alpha} c_{i\beta} &= 12\delta_{\alpha\beta},\\
\sum_i m_i c_{i\alpha} c_{i\beta} c_{i\gamma} &= 0,\\
\sum_i m_i c_{i\alpha} c_{i\beta} c_{i\gamma} c_{i\epsilon} &= 4\delta_{\alpha\beta}\delta_{\gamma\epsilon} + 4\delta_{\alpha\gamma}\delta_{\beta\epsilon} + 4\delta_{\alpha\epsilon}\delta_{\beta\gamma}.
\end{aligned} \tag{A1}$$

The mass density can be obtained by the zeroth-order moment of N_i,

$$\begin{aligned}
\sum_i N_i &= \frac{\rho_l}{24}\sum_i m_i + \frac{\rho_l u_\alpha}{12}\sum_i m_i c_{i\alpha} + \frac{\rho_l u_\alpha u_\beta}{8}\sum_i m_i c_{i\alpha} c_{i\beta}\\
&\quad - \frac{\rho_l u_\alpha u_\alpha}{16}\sum_i m_i - \frac{\rho_l \nu_l}{4}\partial_\alpha \sum_i m_i c_{i\alpha} c_{i\beta} u_\beta + \frac{\rho_l \nu_l}{8}\partial_\alpha \sum_i m_i u_\alpha\\
&= \frac{\rho_l}{24}(24) + \frac{\rho_l u_\alpha}{12}(0) + \frac{\rho_l u_\alpha u_\beta}{8}(12\delta_{\alpha\beta})\\
&\quad - \frac{\rho_l u_\alpha u_\alpha}{16}(24) - \frac{\rho_l \nu_l}{4}\partial_\alpha(12\delta_{\alpha\beta})u_\beta + \frac{\rho_l \nu_l}{8}\partial_\alpha(24)u_\alpha\\
&= \rho_l.
\end{aligned} \tag{A2}$$

Similarly, the momentum concentration is obtained by the first-order moment of N_i,

$$\begin{aligned}
\sum_i \mathbf{c_i} N_i &= \frac{\rho_l}{24}\sum_i m_i c_{i\alpha} + \frac{\rho_l u_\alpha}{12}\sum_i m_i c_{i\alpha} c_{i\beta} + \frac{\rho_l u_\alpha u_\beta}{8}\sum_i m_i c_{i\alpha} c_{i\beta} c_{i\gamma}\\
&\quad - \frac{\rho_l u_\alpha u_\alpha}{16}\sum_i m_i c_{i\alpha} - \frac{\rho_l \nu_l}{4}\partial_\alpha \sum_i m_i c_{i\alpha} c_{i\beta} c_{i\gamma} u_\beta + \frac{\rho_l \nu_l}{8}\partial_\alpha \sum_i m_i u_\alpha c_{i\beta}\\
&= \frac{\rho_l}{24}(0) + \frac{\rho_l u_\alpha}{12}(12\delta_{\alpha\beta}) + \frac{\rho_l u_\alpha u_\beta}{8}(0)\\
&\quad - \frac{\rho_l u_\alpha u_\alpha}{16}(0) - \frac{\rho_l \nu_l}{4}\partial_\alpha(0)u_\beta + \frac{\rho_l \nu_l}{8}\partial_\alpha(0)u_\alpha\\
&= \rho_l u_\beta = \rho_l \mathbf{u}.
\end{aligned} \tag{A3}$$

The second-order moment of N_i results into

$$\begin{aligned}\sum_i \mathbf{c_i c_i} N_i &= \frac{\rho_l}{24}\sum_i m_i c_{i\alpha}c_{i\beta} + \frac{\rho_l u_\alpha}{12}\sum_i m_i c_{i\alpha}c_{i\beta}c_{i\gamma} + \frac{\rho_l u_\alpha u_\beta}{8}\sum_i m_i c_{i\alpha}c_{i\beta}c_{i\gamma}c_{i\epsilon} \\ &\quad -\frac{\rho_l u_\alpha u_\alpha}{16}\sum_i m_i c_{i\gamma}c_{i\epsilon} - \frac{\rho_l \nu_l}{4}\partial_\alpha \sum_i m_i c_{i\alpha}c_{i\beta}c_{i\gamma}c_{i\epsilon}u_\beta + \frac{\rho_l \nu_l}{8}\partial_\alpha \sum_i m_i u_\gamma c_{i\gamma}c_{i\epsilon} \\ &= \frac{\rho_l}{24}(12\delta_{\alpha\beta}) + \frac{\rho_l u_\alpha}{12}(0) + \frac{\rho_l u_\alpha u_\beta}{8}(4\delta_{\alpha\beta}\delta_{\gamma\epsilon} + 4\delta_{\alpha\gamma}\delta_{\beta\epsilon} + 4\delta_{\alpha\epsilon}\delta_{\beta\gamma}) \\ &\quad -\frac{\rho_l u_\alpha u_\alpha}{16}(12\delta_{\gamma\epsilon}) - \frac{\rho_l \nu_l}{4}\partial_\alpha(4\delta_{\alpha\beta}\delta_{\gamma\epsilon} + 4\delta_{\alpha\gamma}\delta_{\beta\epsilon} + 4\delta_{\alpha\epsilon}\delta_{\beta\gamma})u_\beta \\ &\quad +\frac{\rho_l \nu_l}{8}\partial_\alpha(12\delta_{\gamma\epsilon})u_\alpha \\ &= \frac{\rho_l}{2}\delta_{\alpha\beta} + \frac{1}{2}\rho_l u_\alpha u_\beta \delta_{\alpha\beta}\delta_{\gamma\epsilon} + \frac{1}{2}\rho_l u_\alpha u_\beta \delta_{\alpha\gamma}\delta_{\beta\epsilon} + \frac{1}{2}\rho_l u_\alpha u_\beta \delta_{\alpha\epsilon}\delta_{\beta\gamma} \\ &\quad -\frac{1}{2}u_\alpha u_\alpha \delta_{\gamma\epsilon} - \frac{1}{4}u_\alpha u_\alpha \delta_{\gamma\epsilon} - \rho_l \nu_l \partial_\alpha u_\beta \delta_{\alpha\beta}\delta_{\gamma\epsilon} - \rho_l \nu_l \partial_\alpha u_\beta \delta_{\alpha\gamma}\delta_{\beta\epsilon} \\ &\quad -\rho_l \nu_l \partial_\alpha u_\beta \delta_{\alpha\epsilon}\delta_{\beta\gamma} + \rho_l \partial_\alpha u_\alpha \delta_{\gamma\epsilon} + \frac{1}{2}\rho \partial_\alpha u_\alpha \delta_{\gamma\epsilon} \\ &= \frac{1}{2}\rho_l + \frac{1}{2}\rho_l u_\gamma u_\epsilon + \frac{1}{2}\rho_l u_\epsilon u_\gamma - \frac{1}{4}\rho_l u_\alpha u_\alpha \delta_{\gamma\epsilon} - \rho_l \nu_l \partial_\gamma u_\epsilon \\ &\quad -\rho_l \nu_l \partial_\epsilon u_\gamma + \frac{1}{2}\rho_l \partial_\alpha u_\alpha \delta_{\gamma\epsilon}. \end{aligned} \tag{A4}$$

Transforming Eq. (A4) into vector notation yields

$$\begin{aligned}\sum_i \mathbf{c_i c_i} N_i &= \frac{1}{2}\rho_l + \rho_l \mathbf{uu} - \frac{1}{4}\rho_l \mathbf{uu}\cdot\mathbf{I} - \rho_l \nu_l[\nabla\mathbf{u} + (\nabla\mathbf{u})^T] + \frac{1}{2}\rho_l \nu_l(\nabla\cdot\mathbf{u})\mathbf{I} \\ &= \frac{1}{2}\rho_l[1 - \frac{1}{2}tr(\mathbf{uu})] + \rho_l \mathbf{uu} - \rho_l \nu_l[\nabla\mathbf{u} + (\nabla\mathbf{u})^T] + \frac{1}{2}\rho_l \nu_l(\nabla\cdot\mathbf{u})\mathbf{I}. \end{aligned} \tag{A5}$$

Applying the equation of state in the form

$$P = \frac{1}{2}\rho_l[1 - \frac{1}{2}tr(\mathbf{uu})], \tag{A6}$$

Eq. (A5) becomes

$$\begin{aligned}\sum_i \mathbf{c_i c_i} N_i &= \rho_l \mathbf{uu} - \{-P\mathbf{I} + \rho_l \nu_l[\nabla\mathbf{u} + (\nabla\mathbf{u})^T - \frac{1}{2}(\nabla\cdot\mathbf{u})\mathbf{I}]\} \\ &= \rho_l \mathbf{uu} - \sigma. \end{aligned} \tag{A7}$$

According to the first constraint of Ω_i, mass conservation is satisfied through the zeroth-order moment,

$$\begin{aligned}\sum_i \Omega_i &= \frac{\rho_l}{12}\partial_\alpha \sum_i m_i c_{i\alpha}c_{i\beta}u_\beta - \frac{\rho_l}{24}\partial_\alpha \sum_i m_i u_\alpha + \frac{\mathbf{f}}{12}\sum_i m_i c_{i\alpha} \\ &\quad +\frac{f^\phi}{24}\sum_i m_i + \frac{f^\phi}{12}\sum_i m_i c_{i\alpha}u_\alpha \\ &= \frac{\rho_l}{12}\partial_\alpha(12\delta_{\alpha\beta})u_\beta - \frac{\rho_l}{24}\partial_\alpha(24)u_\alpha + \frac{\mathbf{f}}{12}(0) + \frac{f^\phi}{24}(24) + \frac{f^\phi}{12}(0)u_\alpha \\ &= f^\phi. \end{aligned} \tag{A8}$$

Similarly, the first-order moment of Ω_i must satisfy the second constraint for the momentum conservation,

$$\begin{aligned}\sum_i \Omega_i \mathbf{c_i} &= \frac{\rho_l}{12}\partial_\alpha \sum_i m_i c_{i\alpha} c_{i\beta} c_{i\gamma} u_\beta - \frac{\rho_l}{24}\partial_\alpha \sum_i m_i c_{i\alpha} u_\alpha + \frac{\mathbf{f}}{12}\sum_i m_i c_{i\alpha} c_{i\beta} \\ &\quad + \frac{f^\phi}{24}\sum_i m_i c_{i\alpha} + \frac{f^\phi}{12}\sum_i m_i c_{i\alpha} c_{i\beta} u_\alpha \\ &= \frac{\rho_l}{12}\partial_\alpha(0) u_\beta - \frac{\rho_l}{24}\partial_\alpha(0) u_\alpha + \frac{\mathbf{f}}{12}(12\delta_{\alpha\beta}) + \frac{f^\phi}{24}(0) + \frac{f^\phi}{12}(12\delta_{\alpha\beta}) u_\alpha \\ &= \mathbf{f} + \mathbf{u} f^\phi. \end{aligned} \tag{A9}$$

2. Derivation of the collision operator, solution matrix, and solution vectors

The collision operator Ω_i can be derived by substitution of Eq. (12) into Eq. (9) and expanding the staggered formulation of Eq. (8) up to first-order,[17,18]

$$\begin{aligned} N_i\left(\mathbf{x} \pm \frac{1}{2}\mathbf{c_i}, t \pm \frac{1}{2}\right) &= N_i(\mathbf{x}, t) \pm \frac{1}{2}\mathbf{c_i} \cdot \nabla N_i(\mathbf{x}, t) \pm \frac{1}{2}\partial_t N_i(\mathbf{x}, t) + h.o.t. \\ &= N_i(\mathbf{x}, t) \pm \frac{m_i}{48}\mathbf{c_i} \cdot \nabla \rho_l \pm \frac{m_i \rho_l}{24}(\mathbf{c_i} \cdot \nabla)(\mathbf{c_i} \cdot \mathbf{u}) \\ &\quad \pm \frac{m_i}{48}\partial_t \rho_l \pm \frac{m_i}{24}\mathbf{c_i} \cdot \partial_t \rho_l \mathbf{u} + h.o.t., \end{aligned} \tag{A10}$$

where *h.o.t.* represents higher-order terms containing contributions related to the lattice spacing, the time step, and terms of the form $\mathbf{u} \cdot \nabla \rho_l$ which are negligibly small in the incompressible limit.[18] From Eqs. (5) and (6) with Eq. (A6), using $\partial_t \rho_l = -\rho_l \nabla \cdot \mathbf{u} + f^\phi$ and $\partial_t \rho_l \mathbf{u} = -\frac{1}{2}\nabla \rho_l + \mathbf{f} + \mathbf{u} f^\phi + O(\nabla \mathbf{u}^2, \nabla^2 \mathbf{u})$, Ω_i takes the following form:

$$\Omega_i = \frac{m_i \rho_l}{12}[(\mathbf{c_i} \cdot \nabla)(\mathbf{c_i} \cdot \mathbf{u}) - \frac{1}{2}\nabla \cdot \mathbf{u}] + \frac{m_i}{12}\mathbf{c_i} \cdot \mathbf{f} + \frac{m_i}{24}(1 + 2\mathbf{c_i u}) f^\phi + h.o.t., \tag{A11}$$

which corresponds to the LBE in the form

$$N_i(\mathbf{x} \pm \frac{1}{2}\mathbf{c_i}, t \pm \frac{1}{2}) = N_i(\mathbf{x}, t) \pm \frac{1}{2}\Omega_i(\mathbf{N}). \tag{A12}$$

As suggested by Somers[17] (see also Ref. 18), the time marching of the staggered LBE (Eq. (A12)) can be obtained by a linear transformation into an orthogonal basis of eigenvectors $\langle \mathbf{E_k} \rangle$ of Ω_i. The right-hand side of Eq. (A12) is rewritten in terms of a $n \times n$ matrix E_{ki} and a solution vector $\alpha_k^{\pm}(\mathbf{x}, t)$ as

$$N_i(\mathbf{x} \pm \frac{1}{2}\mathbf{c_i}, t \pm \frac{1}{2}) = \frac{m_i}{24}\sum_{k=1}^{n} E_{ik}\alpha_k^{\pm}(\mathbf{x}, t), \qquad i = 1, \ldots, n. \tag{A13}$$

It has been demonstrated by Somers[17] that the $\mathbf{E_k}$ eigenvectors also contain high-order (non-hydrodynamic) modes. They do not appear directly in the conservation equations and are relaxed throughout the simulation. The treatment of these high-order modes contributes to the enhanced stability at low viscosities of the lattice-Boltzmann scheme used here.[49] In 3D, 18 velocity directions are chosen, i.e., $n = 18$, thence E_{ki} and $\alpha_k^{\pm}(\mathbf{x}, t)$ are obtained by substitution of Eqs. (12) and (A11)

into Eq. (A12),

$$E_{ik} = \begin{bmatrix} 1, & c_{ix}, & c_{iy}, & c_{iz}, \\ 2c_{ix}^2 - 1, & c_{ix}c_{iy}, & 2c_{iy}^2 - 1, & c_{ix}c_{iz}, \\ c_{iy}c_{iz}, & 2c_{iz}^2 - 1, & c_{ix}\left(3c_{iy}^2 - 1\right), & \\ c_{iy}\left(3c_{ix}^2 - 1\right), & c_{ix}\left(2c_{iz}^2 + c_{iy}^2 - 1\right), & & \\ c_{iy}\left(2c_{iz}^2 + c_{ix}^2 - 1\right), & c_{iz}\left(3c_{ix}^2 + 3c_{iy}^2 - 2\right), & & \\ c_{iz}\left(c_{iy}^2 - c_{ix}^2\right), & 3\left(c_{ix}^2 - c_{iy}^2\right)^2 - 2, & \left(c_{ix}^2 - c_{iy}^2\right)\left(1 - 2c_{iz}^2\right) & \end{bmatrix}, \tag{A14}$$

$$\alpha_k^{\pm}(\mathbf{x}, t) = \begin{bmatrix} \rho_l \pm \frac{1}{2}\mathrm{f}^{\phi}, \\ \rho_l u_x \pm \frac{1}{2}\mathrm{f}_x \pm \frac{1}{2}u_x f^{\phi}, \\ \rho_l u_y \pm \frac{1}{2}\mathrm{f}_y \pm \frac{1}{2}u_y f^{\phi}, \\ \rho_l u_z \pm \frac{1}{2}\mathrm{f}_z \pm \frac{1}{2}u_z f^{\phi}, \\ \rho_l u_x u_x + \rho_l(\frac{\pm 1 - 6\nu_l}{6})(2\partial_x u_x), \\ \rho_l u_x u_y + \rho_l(\frac{\pm 1 - 6\nu_l}{6})(\partial_x u_y + \partial_y u_x), \\ \rho_l u_y u_y + \rho_l(\frac{\pm 1 - 6\nu_l}{6})(2\partial_y u_y), \\ \rho_l u_x u_z + \rho_l(\frac{\pm 1 - 6\nu_l}{6})(\partial_x u_z + \partial_z u_x), \\ \rho_l u_y u_z + \rho_l(\frac{\pm 1 - 6\nu_l}{6})(\partial_y u_z + \partial_z u_y), \\ \rho_l u_z u_z + \rho_l(\frac{\pm 1 - 6\nu_l}{6})(2\partial_z u_z), \\ T_1^{\pm}, \quad T_2^{\pm}, \quad T_3^{\pm}, \quad T_4^{\pm}, \quad T_5^{\pm}, \quad T_6^{\pm}, \\ F_1^{\pm}, \quad F_2^{\pm} \end{bmatrix}. \tag{A15}$$

The relaxation of the third-order non-hydrodynamic modes is achieved by imposing $T_i^+ = -0.8T_i^-$ with $i = 1, \ldots, 6$. The fourth-order non-hydrodynamic modes are suppressed by setting them to zero, i.e., $F_1^+ = 0$ and $F_2^+ = 0$. The time marching procedure of the scheme starts with the calculation of α_k^- using the existing macroscopic quantities. The mass density N_i required to perform boundary condition is recovered from α_k^- in the next step, see Eq. (A13). After propagation, N_i is used to calculate α_k^+ (inverse of Eq. (A13)) and completed one evolution in lattice unit. The detailed description of the procedure of marching in time with E_{ik} and $\alpha_k^{\pm}(\mathbf{x}, t)$ can be found in Ref. 18.

APPENDIX B: EXPRESSIONS FOR THE LAGRANGIAN PARTICLE TRACKING MODEL

1. Expressions for the forces acting on a solid particle

Since the fluid and the particles experience effective body forces which relate to the acceleration due to gravity, the net gravity force $\mathbf{F_G}$ acting on each spherical particle is described with contribution from the local-average density of mixture $\bar{\rho} = (1 - \phi_p)\rho_l + \phi_p\rho_p$, see Table I.[50] The effects of the pressure gradient ∇p and the shear stress in the fluid $\nabla \cdot \tau$ on each particle can be formulated by

TABLE I. Expressions for the forces acting on a solid particle.

Force	Closure
$\mathbf{F_G} = \left(\rho_p - \bar{\rho}\right) V_p \mathbf{g}$	...
$\mathbf{F_S} = \rho_l V_p D_t \mathbf{u} + \phi_p \left(\rho_p - \rho_l\right) V_p \mathbf{g}$	...
$\mathbf{F_D} = \frac{3}{8}\frac{m_p}{r_p} g\left(\phi_p\right) C_D \left(\mathbf{u} - \mathbf{V}\right) \lvert\mathbf{u} - \mathbf{V}\rvert$	$C_D = \begin{cases} \frac{24}{Re_p}, & Re_p < 0.5 \\ \frac{24}{Re_p}\left(1 + 0.15 Re_p^{0.687}\right), & 0.5 \le Re_p \le 1000 \\ 0.44, & Re_p > 1000 \end{cases}$ $g\left(\phi_p\right) = \left(1 - \phi_p\right)^{-2.65}$ $C_L = 4.1126 Re_s^{-0.5} f_{C_L}$
$\mathbf{F_L} = \pi \rho_l r_p^3 C_L \left[\left(\mathbf{u} - \mathbf{V}\right) \times \omega\right]$	$f_{C_L} = \begin{cases} \left(1 - 0.3314\beta^{0.5}\right) e^{0.1 Re_p} + 0.3314\beta^{0.5}, & Re_p \le 40 \\ 0.0524\left(\beta Re_p\right)^{0.5}, & Re_p > 40 \end{cases}$ $\beta = 0.5\frac{Re_s}{Re_p}$ $Re_s = \frac{4 r_p^2 \lvert\omega\rvert}{\nu_l}$
$\mathbf{F_A} = \frac{1}{2}\rho_l V_p C_A \partial_t \left(\mathbf{u} - \mathbf{V}\right)$	$C_A = 0.5$

applying the material derivative to the lhs of the local-average momentum equations,

$$D_t\left(\phi_l \rho_l \mathbf{u}\right) = -\phi_l \bigtriangledown p + \phi_l \bigtriangledown \cdot \tau + \phi_l \frac{\mathbf{F_B}}{V}, \tag{B1}$$

with $\mathbf{F_B} = -\phi_{p,d}(\rho_p - \rho_l)\mathbf{g}$ the force per unit volume acting on the fluid derived from domain-average force balance between particles and fluid,

$$N_p V_p \left(\rho_p - \bar{\rho}_d\right)\mathbf{g} = -\left(1 - \phi_{p,d}\right) V \mathbf{F_B}, \tag{B2}$$

where V is the volume of the domain and the subscript d indicates domain-average quantities. Using simple algebraic and applying the continuity equation from Eq. (2) on the term on the lhs, Eq. (B1) becomes

$$\rho_l D_t\left(\mathbf{u}\right) = -\bigtriangledown p + \bigtriangledown \cdot \tau + \frac{\mathbf{F_B}}{V}. \tag{B3}$$

Substituting $\mathbf{F_B}$, Eq. (B3) provides expression for the combined effects of $\bigtriangledown p$ and $\bigtriangledown \cdot \tau$,

$$-\bigtriangledown p + \bigtriangledown \cdot \tau = \rho_l D_t\left(\mathbf{u}\right) + \phi_p \left(\rho_p - \rho_l\right)\mathbf{g}. \tag{B4}$$

Hence, the forces due to stress gradients $\mathbf{F_S}$ acting on particles are found by multiplying the gradients with the particle volume,

$$\mathbf{F_S} = \rho_l V_p D_t\left(\mathbf{u}\right) + \phi_p \left(\rho_p - \rho_l\right) V_p \mathbf{g}. \tag{B5}$$

The effect of other particles on the drag force $\mathbf{F_D}$ is described in term of hindrance function $g(\phi_p)$.[51] Detailed discussion concerning the closure relations can be found in Refs. 21, 33, and 34.

[1] E. Guazzelli, "Sedimentation of small particles: how can such a simple problem be so difficult?," C. R. Mec. **334**, 539–544 (2006).
[2] P. N. Segre, E. Herbolzheimer, and P. M. Chaikin, "Long-range correlations in sedimentation," Phys. Rev. Lett. **79**, 2574–2577 (1997).
[3] P. N. Segre, F. Liu, P. Umbanhowar, and D. A. Weitz, "An effective gravitational temperature for sedimentation," Nature (London) **409**, 594–597 (2001).
[4] M. P. Brenner and P. J. Mucha, "That sinking feeling," Nature (London) **409**, 568–571 (2001).
[5] X. Yin and D. L. Koch, "Hindered settling velocity and microstructure in suspensions of solid spheres with moderate Reynolds numbers," Phys. Fluids **19**, 093302 (2007).
[6] E. Guazzelli and J. Hinch, "Fluctuations and instability in sedimentation," Annu. Rev. Fluid Mech. **116**, 97–116 (2011).

[7] G. K. Batchelor, "Sedimentation in a dilute dispersion of spheres," J. Fluid Mech. **52**, 245 (1972).
[8] J. F. Richardson and W. N. Zaki, "Sedimentation and fluidisation. Part I," Trans. Inst. Chem. Eng. **32**, 35–53 (1954).
[9] R. Di Felice, "The sedimentation velocity of dilute suspensions of nearly monosized spheres," Int. J. Multiphase Flow **25**, 559–574 (1999).
[10] S.-Y. Tee, P. J. Mucha, L. Cipelletti, S. Manley, M. P. Brenner, P. N. Segre, and D. A. Weitz, "Nonuniversal velocity fluctuations of sedimenting particles," Phys. Rev. Lett. **5**, 054501 (2002).
[11] R. E. Caflisch and J. H. C. Luke, "Variance in the sedimenting speed of a suspension," Phys. Fluids **28**, 759–760 (1985).
[12] D. L. Koch, "Hydrodynamic diffusion in a suspension of sedimenting point particles with periodic boundary conditions," Phys. Fluids **9**, 2894–2900 (1994).
[13] N.-Q. Nguyen and A. J. C. Ladd, "Sedimentation of hard-sphere suspensions at low Reynolds number," J. Fluid Mech. **525**, 73–104 (2005).
[14] E. J. Hinch, "Hydrodynamics at low Reynolds number: A brief and elementary introduction," in *Disorder and Mixing*, NATO ASI Series E Vol. 152, edited by E. Guyon, J.-P. Nadal, and Y. Pomeau (Kluwer, Boston, 1988), pp. 43–55.
[15] D. L. Koch, "Hydrodynamic diffusion in dilute sedimenting suspensions at moderate Reynolds numbers," Phys. Fluids A **5**, 1141–1155 (1993).
[16] X. Yin and D. L. Koch, "Velocity fluctuations and hydrodynamic diffusion in finite-Reynolds-number sedimenting suspensions," Phys. Fluids **20**, 043305 (2008).
[17] J. A. Somers, "Direct simulation of fluid flow with cellular automata and the lattice-Boltzmann equation," Appl. Sci. Res. **51**, 127–133 (1993).
[18] J. G. M. Eggels and J. A. Somers, "Numerical simulation of free convective flow using the lattice-Boltzmann scheme," Int. J. Heat Fluid Flow **16**, 357–364 (1995).
[19] T. B. Anderson and R. Jackson, "Fluid mechanical description of fluidized beds. Equations of motion," Ind. Eng. Chem. Fundam. **6**, 527–539 (1967).
[20] K. D. Kafui, C. Thornton, and M. J. Adams, "Discrete particle-continuum fluid modelling of gas-solid fluidised beds," Chem. Eng. Sci. **57**, 2395–2410 (2002).
[21] C. T. Crowe, M. Sommerfeld, and Y. Tsuji, *Multiphase Flows with Droplets and Particles* (CRC, Boca Raton, FL, USA, 1998).
[22] J. J. Derksen and H. E. A. Van den Akker, "Large-eddy simulations on the flow driven by a Rushton turbine," AIChE J. **45**(2), 209–221 (1999).
[23] U. Frisch, B. Hasslacher, and Y. Pomeau, "Lattice-gas automata for the Navier-Stokes equation," Phys. Rev. Lett. **56**, 1505–1508 (1986).
[24] D. d'Humieres, P. Lallemand, and U. Frisch, "Lattice-gas automata for the Navier-Stokes equation," Europhys. Lett. **2**, 291–297 (1986).
[25] S. Chen and G. D. Doolen, "Lattice Boltzmann method for fluid flow," Annu. Rev. Fluid Mech. **30**, 329–364 (1998).
[26] A. ten Cate, C. H. Nieuwstad, J. J. Derksen, and H. E. A. Van den Akker, "Particle imaging velocimetry experiments and lattice-Boltzmann simulations on a single sphere settling under gravity," Phys. Fluids **14**, 4012–4025 (2002).
[27] E. Climent and M. R. Maxey, "Numerical simulations of random suspensions at finite Reynolds numbers," Int. J. Multiphase Flow **29**, 579–601 (2003).
[28] D. M. Snider, "An incompressible three-dimensional multiphase particle-in-cell model for dense particulate flows," J. Comput. Phys. **170**, 523–549 (2001).
[29] J. J. Derksen, "Numerical simulation of solids suspension in a stirred tank," AIChE J. **49**, 2700–2714 (2003).
[30] J. Pozorski and S. V. Apte, "Filtered particle tracking in isotropic turbulence and stochastic modeling of subgrid-scale dispersion," Int. J. Multiphase Flow **35**, 118–128 (2009).
[31] M. L. Ekiel-Jezewska, B. Metzger, and E. Guazzelli, "Spherical cloud of point particles falling in a viscous fluid," Phys. Fluids **18**, 038104 (2006).
[32] R. Sungkorn, J. J. Derksen, and J. G. Khinast, "Modeling of turbulent gas-liquid bubbly flows using stochastic Lagrangian model and lattice-Boltzmann scheme," Chem. Eng. Sci. **66**, 2745–2757 (2011).
[33] E. Loth, "Numerical approaches for motion of dispersed particles, droplets and bubbles," Prog. Energy Combust. Sci. **26**, 161–223 (2000).
[34] R. Clift, J. R. Grace, and M. E. Weber, *Bubbles, Drops, and Particles* (Academic, New York, USA, 1978).
[35] B. P. B. Hoomans, J. A. M. Kuipers, W. J. Briels, and W. P. M. Van Swaaij, "Discrete particle simulation of bubble and slug formation in a two-dimensional gas-fluidised bed: A hard-sphere approach," Chem. Eng. Sci. **51**, 99–118 (1996).
[36] E. Guazzelli, "Evolution of particle-velocity correlations in sedimentation," Phys. Fluids **13**, 1537–1540 (2001).
[37] G. Bernard-Michel, A. Monavon, D. Lhuillier, D. Abdo, and H. Simon, "Particle velocity fluctuations and correlation lengths in dilute sedimenting suspensions," Phys. Fluids **14**, 2339–2349 (2002).
[38] P. J. Mucha and M. P. Brenner, "Diffusivities and front propagation in sedimentation," Phys. Fluids **12**, 1305 (2003).
[39] M. P. Brenner, "Screening mechanisms in sedimentation," Phys. Fluids **11**, 754–772 (1999).
[40] H. Nicolai and E. Guazzelli, "Effect of the vessel size on the hydrodynamic diffusion of sedimenting spheres," Phys. Fluids **7**, 3–5 (1995).
[41] D. L. Koch and E. S. G. Shaqfeh, "Screening in sedimenting suspensions," J. Fluid Mech. **224**, 275–303 (1991).
[42] A. J. C. Ladd, "Effects of container walls on the velocity fluctuations of sedimenting spheres," Phys. Rev. Lett. **88**, 048301 (2002).
[43] D. Chehata Gomez, L. Bergougnoux, E. Guazzelli, and J. Hinch, "Fluctuations and stratification in sedimentation of dilute suspensions of spheres," Phys. Fluids **21**, 093304 (2009).
[44] L. Zaichik, V. M. Alipchenkov, and E. Sinaiski, *Particles in Turbulent Flows* (Wiley-VCH, Weinheim, Germany, 2008).
[45] S. E. Elgobashi, "On predicting particle-laden turbulent flows," Appl. Sci. Res. **52**, 309–329 (1994).

[46] O. A. Druzhinin and S. E. Elgobashi, "A Lagrangian-Eulerian mapping solver for direct numerical simulation of bubble-laden turbulent shear flows using the two-fluid formulation," J. Comput. Phys. **154**, 174–196 (1999).
[47] N. G. Deen, M. Van Sint Annaland, M. A. Van der Hoef, and J. A. M. Kuipers, "Review of discrete particle modeling of fluidized beds," Chem. Eng. Sci. **62**, 28–44 (2007).
[48] M. A. Van der Hoef, M. Van Sint Annaland, N. G. Deen, and J. A. M. Kuipers, "Numerical simulation of dense gas-solid fluidized beds: A multiscale modeling strategy," Annu. Rev. Fluid Mech. **40**, 47–70 (2008).
[49] J. J. Derksen, "Simulations of lateral mixing in cross-channel flow," Comput. Fluids **39**, 1058–1069 (2010).
[50] J. J. Derksen and S. Sundaresan, "Direct numerical simulations of dense suspensions: wave instabilities in liquid-fluidized beds," J. Fluid Mech. **587**, 303–336 (2007).
[51] R. Di Felice, "The voidage function for fluid-particle interaction systems," Int. J. Multiphase Flow **20**, 153–159 (1994).